CZECH TECHNICAL UNIVERSITY IN
PRAGUE

Faculty of Nuclear Sciences and Physical
Engineering

Department of Physics

Diploma thesis

Non-photonic reconstruction in heavy-ion collisions

Bc. Jan Vaněk

Supervisor: Mgr. Jaroslav Bielčík, Ph.D.

Prague, 2017

Katedra: fyziky *Akademický rok:* 2016/2017

ZADÁNÍ DIPLOMOVÉ PRÁCE

Student: Bc. Jan Vaněk

Studijní program: Aplikace přírodních věd

Obor: Experimentální jaderná a částicová fyzika

Název práce:
(česky) Rekonstrukce nefotonických elektronů v jádro-jaderných srážkách

Název práce:
(anglicky) Non-photonic reconstruction in heavy-ion collisions

Pokyny pro vypracování:

1) Fyzika těžkých vůní v experimentu STAR a ALICE
2) Detektor STAR
3) Kontrola kvality experimentálních údajů
4) Selekce elektronů ve srážkách Au+Au
5) Korekce na geometrickou akceptanci detektoru a účinnost rekonstrukce elektronů
6) Spektrum nefotonických elektronů
7) Diskuze a závěr

Doporučená literatura:

[1] R. Vogt: Ultrarelativistic Heavy-Ion Collisions, Elsevier, 2007

[2] O. Rusňáková: Fyzika těžkých kvarků na experimentu STAR., Dizertační práce, FJFI ČVUT, 2015

[3] ALICE Collaboration: Measurement of beauty-hadron decay electrons in Pb–Pb collisions at 2.76 TeV with ALICE, J. Phys. Conf. Ser. 612, 012037 (2015)

[4] ALICE Collaboration: Measurement of electrons from beauty hadron decays in pp collisions at 7 TeV, Phys. Lett. B 721, 1 (2013)

[5] A. Andronic, et al.: Heavy-flavour and quarkonium production in the LHC era: from proton–proton to heavy-ion collisions, Eur. Phys. J. C 76, 107 (2016)

Jméno a pracoviště vedoucího diplomové práce:

Mgr. Jaroslav Bielčík, Ph.D., Katedra fyziky, Fakulta jaderná a fyzikálně inženýrská, ČVUT v Praze

Datum zadání diplomové práce: 20.10.2016

Termín odevzdání diplomové práce: 05.05.2017

Doba platnosti zadání je dva roky od data zadání.

....
vedoucí katedry   *děkan*

V Praze dne   20.10.2016

Prohlášení:

Prohlašuji, že jsem svou bakalářskou práci vypracoval samostatně a použil jsem pouze podklady (literaturu, software, atd.) uvedené v přiloženém seznamu.

Nemám závažný důvod proti užití tohoto školního díla ve smyslu 60 Zákona .121/2000 Sb., o právu autorském, o právech souvisejících s právem autorským a o změně některých zákonů (autorský zákon).

V Praze dne 04. 05. 2017   Jan Vaněk

Title:
Non-photonic reconstruction in heavy-ion collisions

Author: Bc. Jan Vaněk

Specialization: Experimental nuclear and particle physics

Sort of project: Diploma thesis

Supervisor: Mgr. Jaroslav Bielčík, Ph.D., Physics department, Faculty of nuclear sciences and physical engineering, Czech technical university in Prague

Abstract: Non-photonic electrons are electrons from semi-leptonic decays of the open heavy-flavor mesons, i.e. D and B mesons. These mesons are produced in early stage of ultra-relativistic heavy-ion collisions and are used as a probe to the quark-gluon plasma which is created in later phase of such collisions. The non-photonic electrons are currently studied at the STAR experiment in Au+Au collisions at $\sqrt{s_{NN}} = 200\,\mathrm{GeV}$ from the year 2014 when a new inner tracking system, the heavy-favor tracker, was installed into the STAR detector which allowed to measure decay vertex of the D and B mesons. The main motivation of this thesis is determination of the contribution of electrons from decay of the B mesons to the total non-photonic electrons yield. Individual steps of the non-photonic electrons analysis are presented and discussed in this thesis.

Key words: Heavy-ion collisions, non-photonic electrons, open heavy-flavor mesons, quark-gluon plasma, STAR experiment

Název práce:
Rekonstrukce neforonických elektronů v jádro-jaderných srážkách

Autor: Bc. Jan Vaněk

Obor: Experimentální jaderná a částicová fyzika

Typ práce: Diplomová práce

Školitel: Mgr. Jaroslav Bielčík, Ph.D., Katedra fyziky, Fakulta jaderná a fyzikálně inženýrská, České vysoké učení technické v Praze

———————————————————————————

Abstrakt: Nefotonické elektrony jsou elektrony ze semileptonických rozpadů těžkých mezonů s otevřenou krásou a půvabem, tj. D a B mezonů. Tyto mezony se tvoří v raném stádiu ultra-relativistických srážek těžkých iontů a používají se jako sonda do kvark-gluonového plazmatu, které se utváří v pozdější fázi takových srážek. V současnosti jsou nefotonické elektrony studovány na experimentu STAR ve srážkách Au+Au při $\sqrt{s_{NN}} = 200\,\text{GeV}$ z roku 2014, kdy byl do detektoru STAR nainstalován nový vnitřní dráhový systém, dráhový detektor těžkých vůní (the heavy-flavor tracker), který umožnil měřit rozpadové vertexy D a B mezonů. Hlavní motivací této práce je stanovení příspěvku elektronů z rozpadů B mezonů k celkovému výtěžku nefotonických elektronů. Jednotlivé kroky analýzy nefotonických elektronů jsou představeny a diskutovány v této práci.

Klíčová slova slova: Jádro-jádrové srážky, nefotonické elektrony, mezony s otevřeným půvabem a krásou, kvark-gluonové plazma, experiment STAR

Acknowledgement

Contents

List of Figures

List of Tables

Introduction

Strongly interacting particles, the quarks and gluons, are trapped inside colorless hadrons in contemporary Universe. This property of the strong interaction is referred as color confinement. Non-perturbative space-time Lattice QCD (Quantum Chromo-Dynamics) calculations predict cross-over phase transition from confined hadronic matter to phase called the Quark-Gluon Plasma (QGP), which occurs at temperature approx. 170 MeV and baryon chemical potential $\mu_B \rightarrow 0$ MeV [1]. In this QGP phase the quarks and gluons are no longer bound inside hadrons. It is believed that the QGP was present in the Universe about 10^{-5} s after the Big Bang [2].

The QGP can be experimentally studied via ultra-relativistic heavy-ion collisions. Large synchrotron accelerators and colliders are used for accelerating and colliding heavy ions, where two most powerful and well known are the Relativistic Heavy Ion Collider (RHIC) in Brookhaven National Laboratory, Long Island, USA and the Large Hadron Collider (LHC) in CERN laboratory near Geneva, Switzerland. The experiments dedicated predominantly to study of the QGP and heavy-ion collisions are the ALICE (A Large Ion Collider Experiment) at the LHC and the STAR (Solenoidal Tracker At RHIC) with the PHENIX[1] (Pioneering Hight Energy Nuclear Interaction eXperiment) experiment at the RHIC.

Signatures of the QGP in heavy-ion collisions at the STAR experiment and other experiments are based on comparison of heavy-ion data with proton-proton data, where it is assumed that no QGP is present. Also other colliding systems are used for comparison, such as proton-ion or deuteron-ion collisions which provide information about so-called cold nuclear matter effects. The three most discussed effects observed in heavy-ions collisions, which are considered to be evidence of presence of the QGP are: the quarkonium production suppression in heavy-ion collision, the asymmetry in transverse momentum p_T spectrum called collective flow, and the high p_T particles suppression, which is also referred as jet-quenching. However, it is important to note that similar phenomenons were observed also in high multiplicity p+p or p+ion collisions.

All these phenomenons can be measured either for all particles produced in the collision, or it is possible to focus on specific particle species. For example, it is interesting to study open heavy-flavor mesons, i.e. D mesons, containing c quark and B mesons, containing b quark, as they both are good probe to the QGP. Due to large masses of c and b quarks, they are produced predominantly in initial phase of the heavy-ion collision, during the hard scattering, before ignition of the QGP fireball. Therefore they have to pass thorough the fireball, where they interact with the surrounding medium, and so they carry information about the QGP.

Unfortunately the D and B mesons have short lifetime and can not be detected directly. The only option is to measure their decay products. Two most used decay channels of the open heavy-flavor mesons are the hadronic channel, where all decay products are hadrons, and the semi-leptonic channel, where one product is charged lepton, the second is corresponding neutrino and the rest is one or more hadrons. When using the semi-leptonic channel, usually only decays with electrons are used as electrons are relatively easy to detect and collider experiments at RHIC and LHC have means to distinguish them from other charged particles, mainly pions, kaons and protons. In case of the STAR experiment it is the Time Of Flight (TOF) system and Barrel Electro-Magnetic Calorimeter (BEMC). Another benefit of this channel is that only one decay product is reconstructed, in contrast with hadronic channel, where all decay products have to

---

[1]The PHENIX experiment finished data taking in the year 2016 and is currently being upgraded to sPHENIX.

be reconstructed. The main disadvantages of the semi-leptonic channel are that it does not provide sufficient information about p_T and kinematics of mother particle and that there is a large background consisting of electrons from other sources and hadrons which were misidentified as electrons.

The electrons from decay of the D and B mesons are referred as non-photonic electrons (NPE). There are two main methods used for the NPE measurement. The firs one is reconstructing the photonic background first and then subtracting it from the inclusive electrons spectrum. The second one is direct reconstruction of the NPE based on measurement of the Distance of Closest Approach to the primary vertex (designated DCA or d_0), which is the closest distance between the primary vertex and the reconstructed electron track, conventionally measured in plane transverse to the collider beam axis. The DCA method requires very good spatial resolution of the detector as it is based on precise reconstruction of the primary and secondary vertex. The main advantage of this method is that it is able to directly distinguish the NPE from D and B mesons, which is not possible with the background subtraction method.

The DCA method analysis of Run14 (from the year 2014) Au+Au at $\sqrt{s_{NN}} = 200$ GeV data measured by the STAR experiment is presented in this thesis. The goal of the thesis is to provide detailed description of individual steps of the DCA method. Each step of the analysis was done by me with certain amount of help from other STAR collaboration members, mainly from STAR NPE group. The data analysis, where inclusive electrons were reconstructed, was done using standard software developed by the STAR collaboration for reading PicoDst data files. The cuts and code were then adopted and extended by me so that only relevant data for this analysis were saved.

The second step were the simulations of D and B mesons and photonic background templates for the template fitting of the DCA distributions from data. The templates for D and B mesons were generated using StarEvtGen + Data-driven fast simulator developed by STAR collaboration and adopted for the NPE study by STAR NPE group. Different methods for improving the shape of the D and B templates are to be implemented. The photonic background template was obtained from full HIJING simulation.

The third step of the analysis is the fit of the simulated templates to the experimental data. The code used for fitting was developed entirely by myself using the ROOT TFractionFitter class which was chosen for testing of the templates. For reasons discussed in chapter 4, another fitting method using the TMinuit ROOT class with χ^2 test is currently being developed.

As the STAR collaboration member, I also participated on data taking by the STAR experiment in the year 2016 and 2017 by serving four weeks as a detector operator (two weeks in 2016 and two weeks in 2017). I also plan to present my results at upcoming STAR regional meeting 2017 which will be held in June in Warsaw, Poland. It is also important to stress that my analysis is similar to the one currently being performed by the STAR NPE group. Members of the STAR NPE group presented their preliminary results on the QM 2017 conference in Chicago.

Chapter 1

Heavy-ion collisions

Ultra-relativistic heavy-ion collisions are one of the main experimental tools for measurement of an extreme state of matter known as the quark-gluon plasma (QGP). In this chapter there are three sections where the first is about physical motivation for the heavy-ion collisions, the second is about properties of the heavy-ion collisions and the third provides summary of experimental signatures of the QGP in heavy-ion collisions.

1.1 Physical motivation

Heavy-ion collisions are used for study of the nuclear matter. The goal is to describe the nuclear matter using the theory of strong interaction, the quantum chromo-dynamics (QCD). In many theoretical QCD calculations and models the nuclear matter is usually approximated by infinite volume of protons and neutrons with finite ratio between them.

One of the goals of the QCD is to understand phase diagram of the nuclear matter. Example of schematic phase diagram can be seen in Fig. 1.1, where the calculations were performed mostly using Lattice-QCD with different initial conditions. On the y axis there is temperature T and on the x axis there is baryon-chemical potential μ_B. The shaded area represents anticipated first order transition [3], the dashed line at low μ_B is cross-over transition which occurs at critical temperature $T_{crit} \approx 170$ MeV for $\mu_B \to 0$ MeV [1] and E is the critical point [4]. Point M marks state of nuclear matter present inside atomic nuclei and the remaining points represent place of chemical freeze-out (see Section 1.2.2) calculated from statistical model [5].

There are three phases of nuclear matter plotted in Fig. 1.1. The first one is hadronic phase at lower T and μ_B in which quarks and gluons are trapped inside colorless hadrons. This state of nuclear matter arises from property of strong interaction called color confinement and it is dominant for hadronic matter in the contemporary Universe. The second one is the color super-conductor [6] which appears at low T and high μ_B (i.e. at high hadronic density). Protons and neutrons are fermions and in hadronic phase they have to obey Fermi statistics, but in this phase they combine into so-called Cooper pairs which follow Bose-Einstein statistics so the whole system can "fall" to a lower energetic state. This mechanism is very similar to the one observed in metallic super-conductors where the Cooper pairs are formed by electrons.

The last phase is the QGP which is the most important in context of heavy-ion collisions. In the QGP the quarks and gluons are no longer confined inside hadrons, hence this phase is also referred as deconfinement. Quarks and gluons inside the QGP are not completely free as they still interact via strong interaction. It is believed that the QGP was present in very early stage of the Universe, to be more specific approx. 10^{-5} s after the Big Bang [2], so study of heavy-ion collisions, in which the QGP is produced, also provides information about history of the Universe.

The main accelerators with heavy-ion programe are the Large Hadron Collider (LHC) in CERN Laboratory near Geneva, Switzerland and the Relativistic Heavy-Ion Collider (RHIC) in Brookhaven National Laboratory, Long Island, USA. When they operate at their top energy of
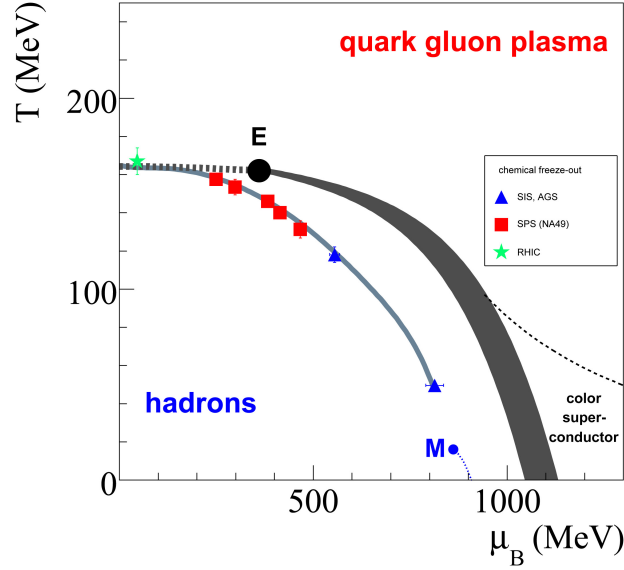
Fig. 1.1: Phase diagram of nuclear matter. On the y axis there is temperature T and on the x axis there is baryon-chemical potential μ_B. The shaded area represents anticipated first order transition, the dashed line at low μ_B is cross-over transition and E is critical point. Point M marks state of nucl. matter present inside atomic nuclei and the remaining points represent place of chemical freeze-out (see Section 1.2.2) calculated from statistical model. Individual phases of nuclear matter are denoted in the plot. Taken from Ref. [7].

collisions, they both explore the part of the phase diagram where $\mu_B \to 0$ MeV, so all transitions observed in such collisions are cross-overs which occur at T_{crit}. The RHIC has an advantage, compared to the LHC, that the collision energy can be varied more flexibly and so it can scan the phase diagram in more detail.

Example of such measurement is an attempt to prove existence of the critical point by the STAR experiment in Ref. [8]. The net-proton multiplicity ΔN ($\Delta N = N_p - N_{\overline{p}}$ where N_p and $N_{\overline{p}}$ is number of protons and antiprotons respectively) was studied in Au+Au collisions in range of collision energies from $\sqrt{s_{NN}} = 7.7$ GeV to $\sqrt{s_{NN}} = 200$ GeV. The ΔN is expected to follow Skellam distribution far from critical point and theoretical calculations predict ΔN fluctuations close to the critical point [9]. As can be seen if Fig. 1.2, deviation from Skellam distribution for ΔN was observed with decreasing collision energy which suggests existence of the critical point.

To conclude, the main goals of study of the heavy-ion collisions is to determine properties of the QGP and the transitions between the QGP and normal (confined) hadronic matter. So far, it is experimentally proven that at low μ_B and temperature $T_{crit} \approx 170$ MeV the transition is cross-over and that the critical point possibly exists [8]. Other properties of the phase diagram, such as exact position of the critical point, are sill to be determined.

Fig. 1.2: Net-proton multiplicity in Au+Au collisions measured by the STAR experiment. Skewness S and kurtosis κ of the net-proton multiplicity are plotted as a function of collision energy $\sqrt{s_{NN}}$. The σ is standard deviation. Taken from Ref. [8].

1.2   General characteristics of heavy-ion collisions

1.2.1   Geometry

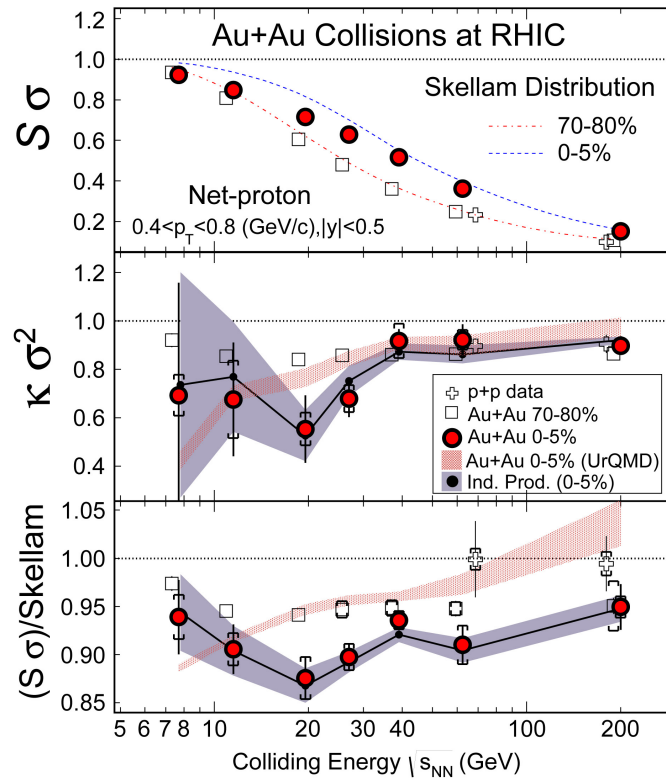Heavy ions used in accelerators are relatively large objects and it is not possible to neglect their size. Signal from each individual collision of two nuclei is strongly dependent on initial collision geometry. One of the main geometry characteristics is the centrality which is basically distance between centres of the two nuclei in plane perpendicular to their movement. This distance is referred as the impact parameter b and is schematically shown in Fig. 1.3. When $b \approx 0$ fm the collision is called central, when $b \to 2R$, where R is radius of the colliding nuclei, then it is called peripheral.
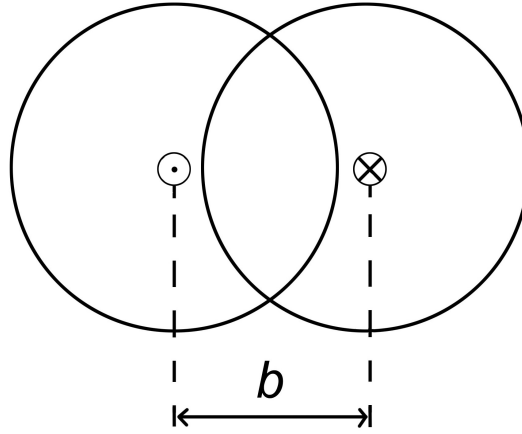
Fig. 1.3: Scheme of heavy-ion collision in plane perpendicular to the movement of the nuclei. The distance between the centres of the projectiles is called impact parameter b.

The centrality is usually parameterised by number of participants N_{part}, which is number of nucleons from both colliding nuclei that participated in given collision. The remaining nucleons are called spectators, which keep on going after the collision. The N_{part} can not be measured directly, but the spectators can be detected by so called zero-degree calorimeters (ZDC) which are usually placed relatively far form interaction point, close to the beam axis. The ZDC basically measures the number of spectators which can be relatively easily used for N_{part} determination because total number of nucleons in colliding nuclei is known.

It is also convenient to define system of coordinates. By convention it is right-handed Cartesian system where the z axis is parallel to the beam axis, the x axis is horizontal and y axis is vertical, as shown in Fig. 1.4. Azimuthal angle ϕ is measured in x-y plane from the x axis (also shown in Fig. 1.4), longitudinal angle θ is measured form the z axis, but is is not used very often. Pseudorapidity η defined as

$$\eta = -\ln\left[\tan\left(\frac{\theta}{2}\right)\right] \tag{1.1}$$

is usually used instead.

When two nuclei collide, the line connecting their centres (projected to the x-y plane) is not generally parallel to the x axis as shown in the Fig. 1.4. For that reason a reaction plane is used which is a plane parallel to the beam axis (z axis) and contains centres of both colliding nuclei.
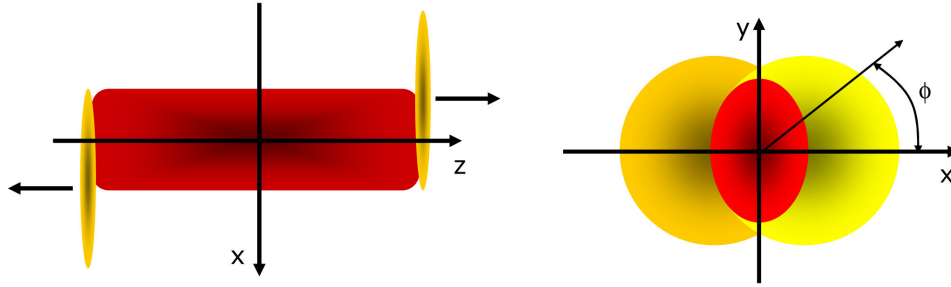
Fig. 1.4: System of coordinates in a heavy-ion collision. The z axis is parallel to the beam axis, the x axis is horizontal and y axis is vertical. Taken from Ref. [10].

1.2.2 Space-time evolution
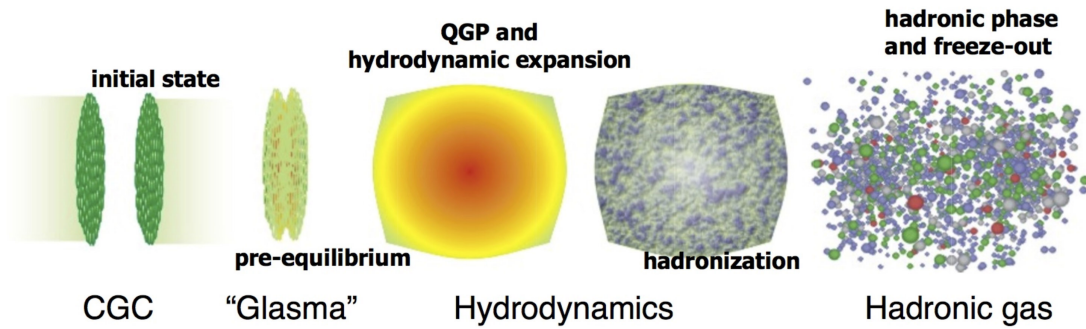
Fig. 1.5: Individual pases of a heavy-ion collision. The individual phases are denoted in the figure. For more detailed description see the text. Taken from Ref. [11].

The heavy-ion collision can be divided into several phases, which are shown in Fig. 1.5. In the initial state the nuclei are far apart and they do not interact with each other. Theoretical description of the initial state is still not completely resolved but one of the most used models today is the color-glass condensate (CGC) [12]. The colliding nuclei are travelling at ultra-relativistic speed hence they are relativistically contracted and they appear as discs in the laboratory system. The CGC describes these discs as fragile walls made (predominantly) of gluons.

The primary interaction of the nucleons of the two colliding nuclei is called the hard scattering and it is the phase of the heavy-ion collision where particles with high p_T are created. Very shortly after the hard scattering, probably less than 1 fm/c [11], a fireball of QGP is ignited. The fireball expands following relativistic viscous hydrodynamics until its temperature falls down to critical temperature T_{crit}. At this point deconfinement can not be present any more and the fireball hadronizes.

The hadronization process is a complex event with multiple stages, as shown in Fig. 1.6. After cooling down under the critical temperature T_{crit} (T_c in Fig. 1.6), there is a mixture of strongly interacting hadrons whose species can change. The volume is further increasing and the temperature dropping down to temperature of chemical freeze-out T_{ch}, under which the hadrons are interacting with each other, but the composition of the hadron gas remains unchanged. T_{ch} is very likely close to T_{crit}. As the volume increases even more the temperature drops below temperature of kinetic freeze-out T_{fo} under which the hadrons do not interact with each other and the composition remains unchanged.
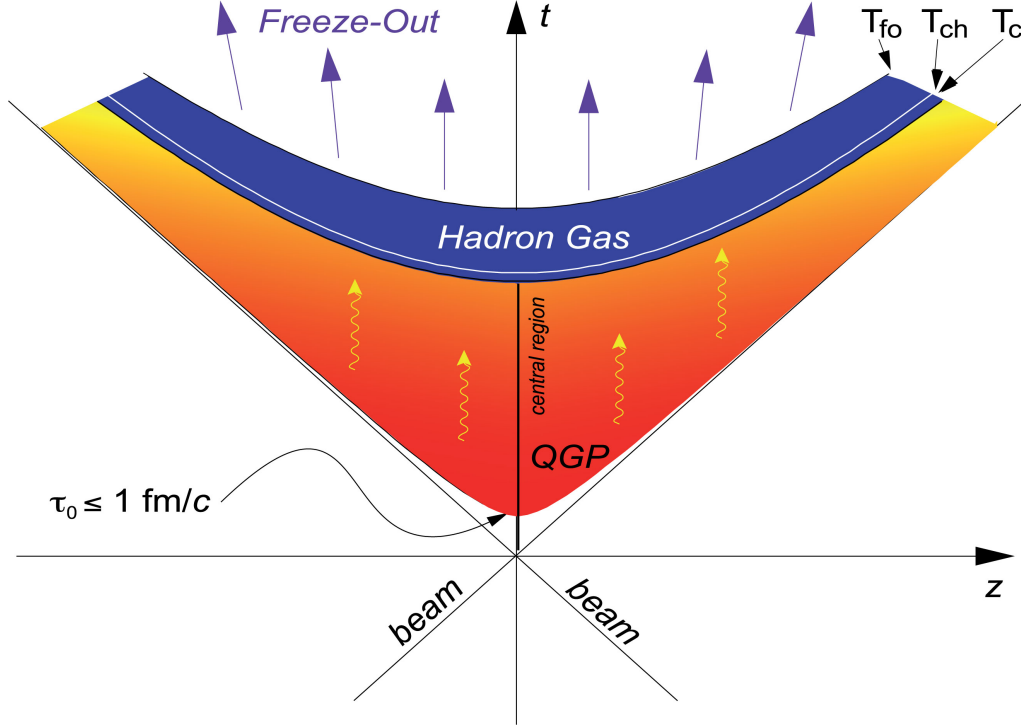
Fig. 1.6: Diagram of the time evolution of a heavy-ion collision, where z is the beam axis, t is time, T_c is critical temperature (in text denoted T_{crit}), T_{ch} is temperature of chemical freeze-out and T_{fo} is temperature of kinetic freeze-out. For more detailed description see the text. Taken from Ref. [7].

1.3   Experimental signatures of the QGP

There are several signals proving existence of the QGP in heavy-ion collisions. In this section examples of most important signals are presented. They are particle production suppression in heavy-ion collisions compared to proton-proton collisions, elliptic flow and higher order harmonics and finally so called jet quenching and dead-cone effect.

1.3.1   Particle production suppression

Particle production suppression in heavy-ion collisions is quantified by nuclear modification factor R_{AA} defined as (taken from Ref. [13])

$$R_{AA}(p_T) = \frac{\mathrm{d}N_{ch}^{AA}(p_T)/\mathrm{d}p_T}{\langle N_{coll}\rangle \mathrm{d}N_{ch}^{pp}(p_T)/\mathrm{d}p_T}, \tag{1.2}$$

where N_{ch}^{AA} is number of charged particles created in given heavy-ion collision, N_{ch}^{pp} is number of charged particles created in given proton-proton collision and $\langle N_{coll}\rangle$ is mean number of binary (parton-parton) collisions in heavy-ion collision. This variable is defined so that if heavy-ion collision were simple superposition of individual binary collisions, the R_{AA} would be equal to unity. In other words, $R_{AA} = 1$ would mean, that there is either no QGP created in studied collision or other effects in given collision compensate the QGP effects.

Experimental results show that R_{AA} is below unity for all p_T at LHC and RHIC. Example of such measurement for light and inclusive hadrons is in Fig. 1.7, where the data come from multiple experiments at RHIC (BNL), SPS and LHC (CERN). At the SPS the data are consistent with $R_{AA} = 1$, i.e. no suppression is observed. At higher collision energy at the RHIC a significant

Fig. 1.7: Nuclear modification factor R_{AA} as function of p_T. Shown are data from multiple experiments at RHIC (BNL), SPS and LHC (CERN). Comparison with multiple models is also plotted. Taken from Ref. [14].

suppression is observed for transverse momentum in range approx. $5 < p_T < 20 \, \mathrm{GeV}/c$. Particles in this p_T range come, very likely, primarily from the hard scattering, so their suppression suggests presence of a medium, most likely QGP, in which they loose momentu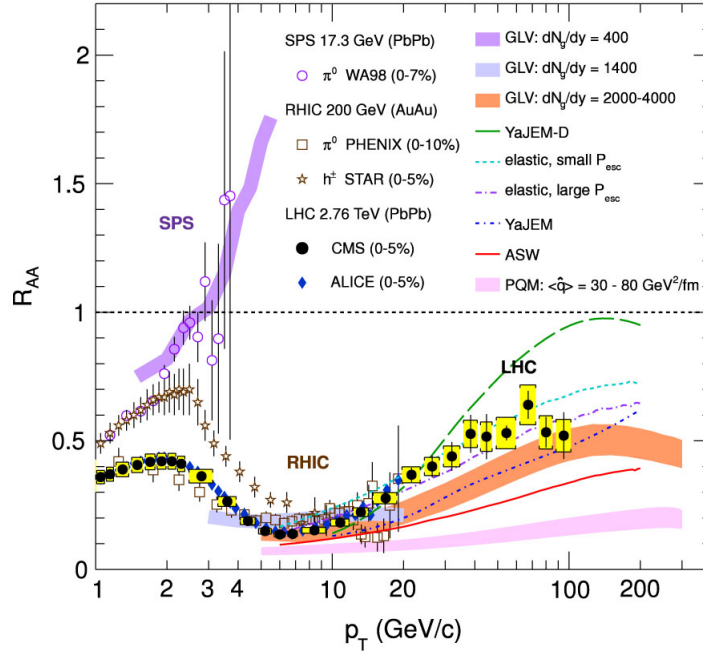m. Higher p_T is reasonably accessible only at the LHC. The LHC data shows that particles with higher p_T are suppressed less than particles with lower p_T which gives gives hit to p_T dependency of the particles energy loss in the QGP. Comparison with multiple models is also plotted[1].

Particles from the hard scattering are good probe to the QGP as the hard scattering takes place in initial state of the heavy-ion collision, before the QGP fireball ignition, and the particles therefore have to travel through the subsequently ignited QGP fireball, where they loose energy and momentum. As a result they can be stopped completely, which means they will not be detected at all.

As it turned out, many of particles produced in heavy-ion collisions come hadronization described in Section 1.2.2 and not the hard scattering. Particles from hadrnonization usually cary relatively low p_T, lets say $p_T < 4 \, \mathrm{GeV}/c$, which is one of reasons why the hump around $2 \, \mathrm{GeV}/c$ is observed in the Fig. 1.7.

In previous example, only light and inclusive hadrons were discussed. It is also beneficial to look at heavy hadrons, mainly at the quarkonia. The quarkonia are mesons which consist of heavy quark and antiquark of the same flavor. Quarkonium (in ground state) containing c quark is the J/ψ (charmonium) and quarkonium containing b quark is the Υ (bottomonium). The quarkonia are used as a thermometer of the QGP as they have well defined bound energy. Information about temperature of the QGP can be obtained by measuring set of different charmonia or bottomonia excited states (ground + higher). More excited states have lower binding energy and therefore are dissolved, due to color screening, at lower temperature of the medium. As the temperature of the QGP rises (e.g. due to higher collision energy), more and more states of the qurkonia is suppressed

---

[1]GLV = Gyulassy-Levai-Vitev, YaJEM = Yet another Jet Energy-Loss Model, ASW = Armesto-Salgado-Wiedemann, PQM = Parton Quenching Model.

by the medium. Example of such measurement by the CMS experiment at the LHC can be seen in Fig. 1.8. The CMS results clearly show that $\Upsilon(2S)$ state is more strongly suppressed in Pb+Pb collisions than $\Upsilon(1S)$ state.
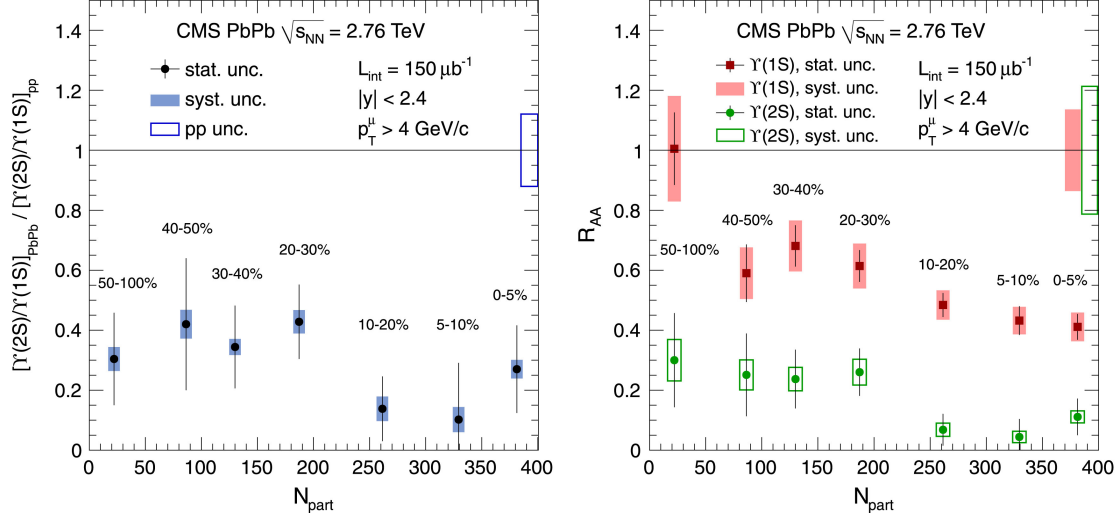

Fig. 1.8: (left) Comparison of yield of $\Upsilon(1S)$ and $\Upsilon(2S)$ states in p+p and Pb+Pb collisions. The result shows that $\Upsilon(2S)$ state is more strongly suppressed in Pb+Pb collisions than $\Upsilon(1S)$ state. (right) Nuclear modification factor R_{AA} for $\Upsilon(1S)$ and $\Upsilon(2S)$ states. The physical message is the same as in case of the left panel. Taken from Ref. [15].

1.3.2   Elliptic flow and higher harmonics

Elliptic flow v_2 and higher order harmonics v_n are asymmetries in p_T azimuthal spectrum of given collision which arise from spatial asymmetry of overlap region of the colliding nuclei. As shown in Fig. 1.9 on the right, the fireball is smaller in direction parallel to the event plane than in direction perpendicular to the event plane. This means that particles in the event plane will obtain higher p_T than the particles out of it, due to higher pressure gradient in the event plane. As the spatial asymmetry can be approximated by an ellipse, the resulting p_T asymmetry will be also elliptical and for that reason is called elliptic flow. The elliptic flow was observed in heavy-ion collisions, which also suggests that the mean free path of the particles inside the fireball is smaller than size of the fireball itself.

$$\frac{\mathrm{d}N}{\mathrm{d}\varphi} \propto 1 + 2\sum_{n=1}^{\infty} v_n \cos[n(\varphi - \Psi_n)] \tag{1.3}$$

Individual harmonic flows v_n are mathematically defined as coefficients of the particle azimuthal distribution Fourier series (1.3) as defined in Ref. [16]. The φ is here the azimuthal angle and the Ψ_n is the n-th order event plane. The Ψ_n is necessary as the n-th order event plane is generally different than event plane of the collision, defined in section 1.2.1, and two event planes of different orders are also not generally identical. Generally the n-td order event plane Ψ_n is defined as a plane in which the particles have highest overall momentum, or alternatively it is the plane in which the pressure gradient inside the fireball is the largest.

Example of measurement of elliptic flow v_2 is shown in Fig. 1.10. The v_2 is here plotted as a function of p_T for several particle species in two centrality bins. The data is also compared to VISHNU model[2]. This plot shows v_2 as a function of p_T for two centrality bins of Pb+Pb

---

[2]Viscous Israel-Steward Hydrodynamics 'n' UrQMD, UrQMD = Utra-relativistic Quantum Molecular Dynamics
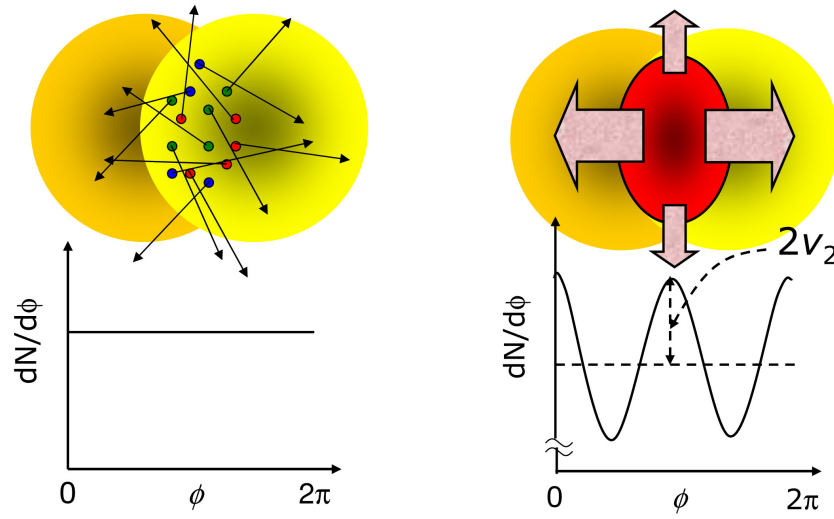
Fig. 1.9: Scheme for demonstration of elliptic flow v_2. On the left is situation when mean free path of particles inside the fireball is larger than the size of the fireball - no elliptic flow is present. On the right is situation when the mean free path of the particles is smaller than the fireball - elliptic flow is present. Taken from Ref. [10].

collisions at $\sqrt{s_{NN}} = 2.76$ TeV measured by the ALICE experiment at the LHC. It is apparent that the v_2 is larger in semicentral collisions than in central collisions and that the expansion of the QGP fireball is well described by relativistic hydrodynamics.

Higher order harmonics arise from more complicated spatial asymmetries of the overlap region than ellipse, such as triangle - triangular flow v_3, etc. The highest order measured to this date was v_6 by ATLAS experiment at LHC. As shown in Ref. [17] higher order harmonics are less significant for higher n for semi-central and peripheral collisions, in central collisions the triangular flow v_3 exceeds the elliptic flow v_2, which is caused by nearly circular overlap of the colliding nuclei where higher order spatial asymmetries can be more significant than the elliptic one.
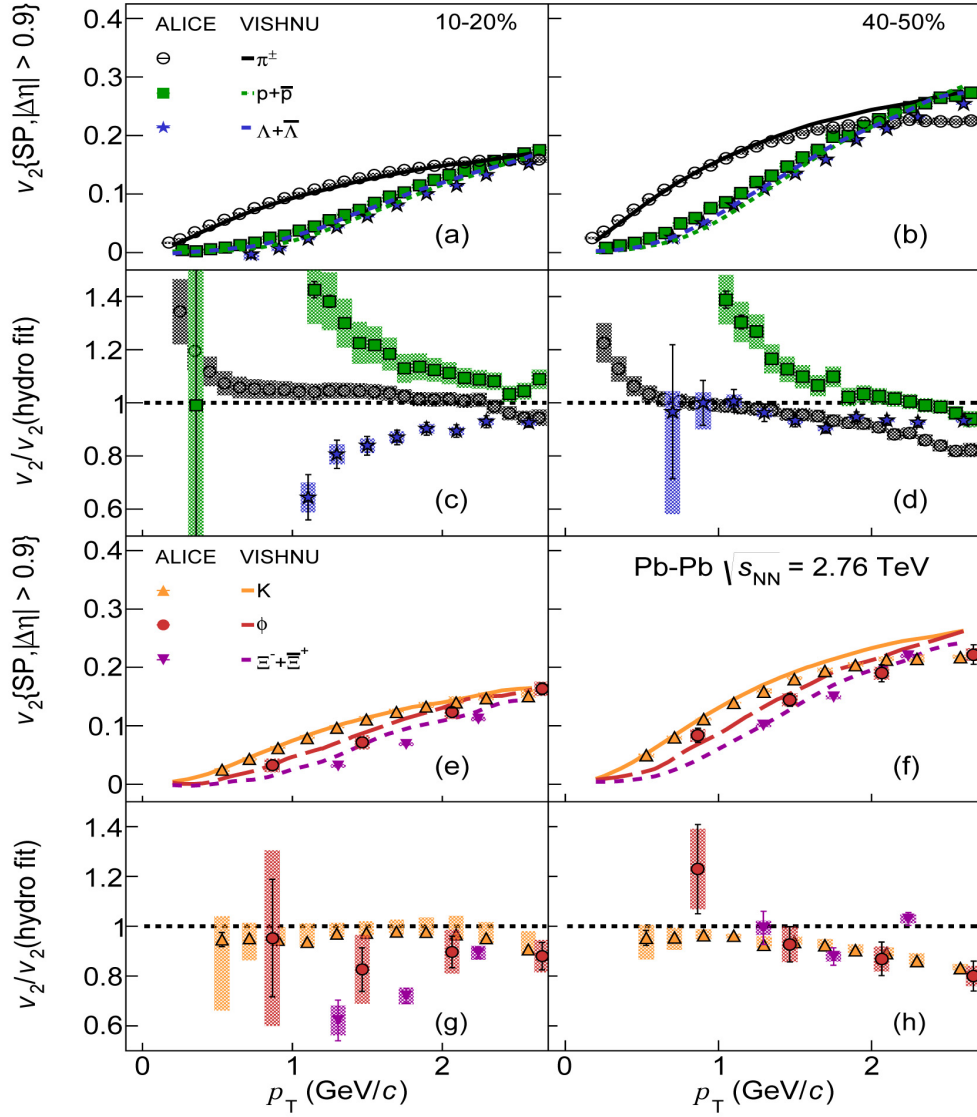
Fig. 1.10: (a), (b), (c), (d): Elliptic flow v_2 as a function of p_T measured by ALICE in Pb+Pb collisions at $\sqrt{s_{NN}} = 2.76$ TeV for multiple particle species and for two centrality bins. VISHNU model (fit) is also plotted. (c), (d), (g), (h): Ratio of experimental data and model. Taken from Ref. [18].

1.3.3   Jet quenching

Collimated, high energy showers of particles are observed in proton-proton and heavy-ion collisions and are called jets. They arise from hadronization of high-energetic partons originating in hard scattering. In proton-proton collisions there is nothing to influence the movement of the daughter partons and therefore the resulting jets can be fully reconstructed. In case of the heavy-ion collision one, or both daughter partons have to travel through the QGP where they loose energy as schematically shown in Fig. 1.11.
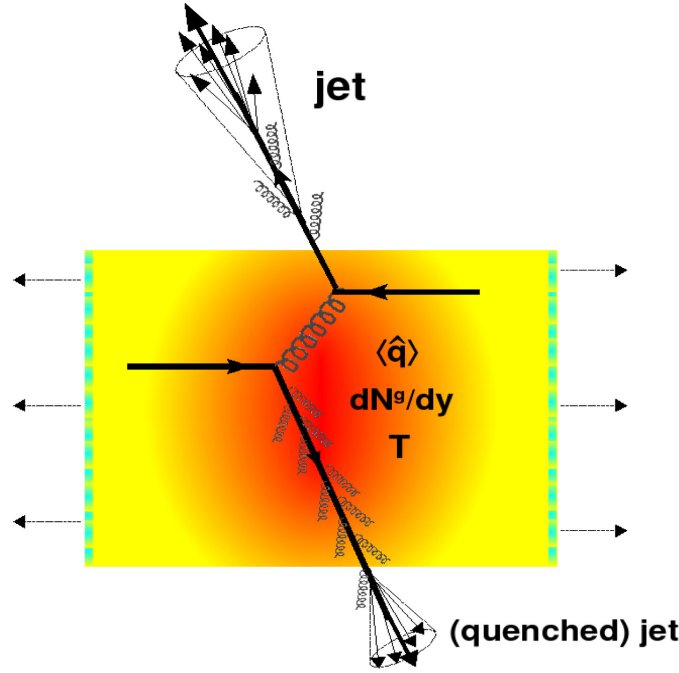
Fig. 1.11: Scheme for demonstration of jet quenching. Taken from Ref. [19]

As a result one of the jets is suppressed compared to the other. The jet with higher energy (or p_T) is called leading or near-side jet and the one with lower energy is subleading or away-side jet. In case the hard scattering occurs close to the edge of the QGP fireball, one of the partons exits the fireball immediately and the other has to go through the whole QGP volume. In this case the away-side jet can be suppressed completely.

Possible way to measure jet quenching is to measure two-particle azimuthal distribution. A high p_T particle is chosen as a trigger, than all particles with lower p_T, in chosen p_T range, associated with the trigger particle (in given event), are selected. The yield of associated particles is subsequently plotted as a function $\Delta\phi$ which is angle between the trigger particle and associated particles. An example of such jet measurement at the STAR experiment is shown in Fig. 1.11. Two particle azimuthal distributions for central Au+Au data (blue stars) and d+Au data for two collision centralities (red circles and green triangles) are compared to p+p data (black histogram). The leading, trigger, particle, at $\phi = 0$, was required to have $4 < p_T(trig) < 6\,\mathrm{GeV}/c$ and only associated particles with $2\,\mathrm{GeV}/c < p_T < p_T(trig)$ were accepted. No jet quenching was observed in d+Au collisions, as can be seen in panel (a). In central Au+Au, on the other hand, the away side jet, at $\Delta\phi = \pi$, is not observed, i.e. it is completely quenched. Measurement presented in Fig. 1.11 is important as it is the first measurement at the STAR experiment where the jet quenching was observed.
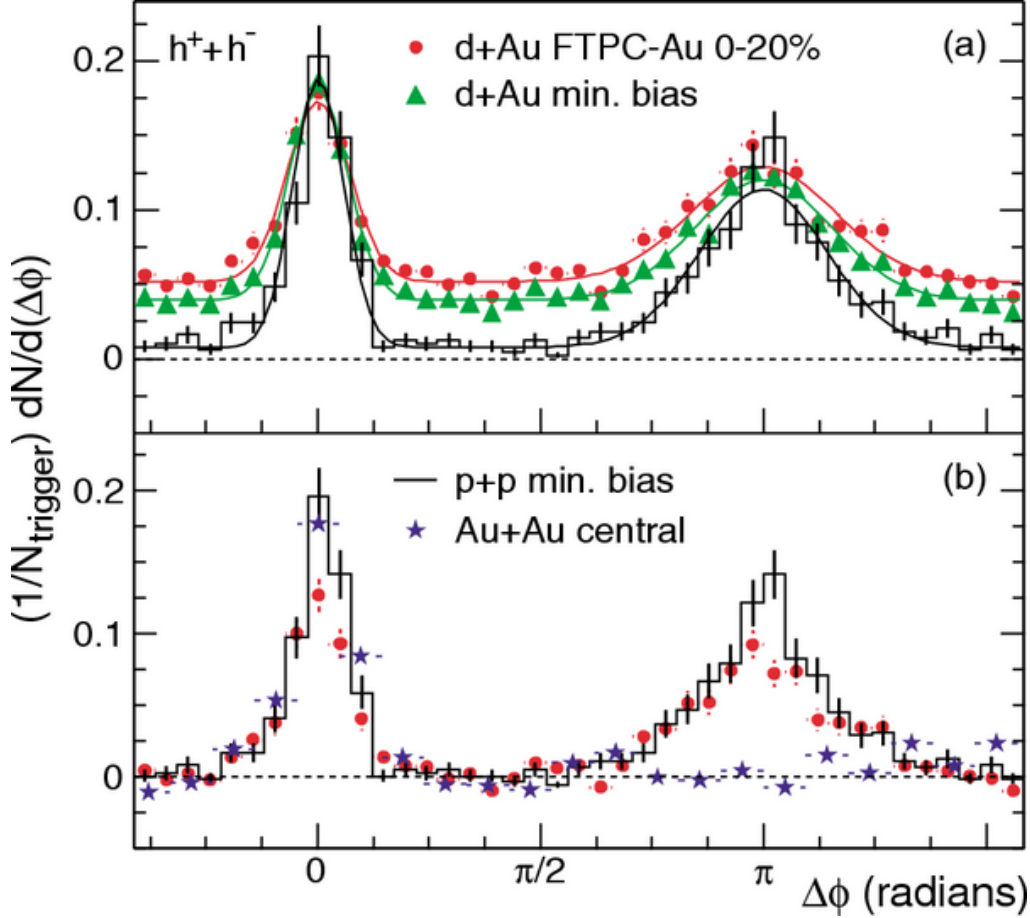
Fig. 1.12: Two-particle (hadron) azimuthal distribution measured by STAR for p+p, d+Au and Au+Au collisions, both at $\sqrt{s_{NN}} = 200$ GeV. The leading, trigger, particle was required to have $4 < p_T(trig) < 6$ GeV/c and only associated particles with 2 GeV/$c < p_T < p_T(trig)$ were accepted. Taken from Ref. [20].

1.3.4   Dead-cone effect

When a fast (high p_T) quark (or strongly interacting particle) is propagating through the QGP it looses large amount of its energy through radiative energy loss, i.e. through the Bremsstrahlung. It turned out that the radiative energy loss is significantly suppressed for quarks in direction of their movement at angle $\theta = \frac{M}{E}$ in approximation of small angles, where θ is angle between the quark and radiated gluon, M is quark mass and E is energy of the quark [21]. This phenomenon is known as the dead-cone effect.

As a result, heavier particles are expected to suffer lower total radiative energy loss in the QGP than lighter. This is supported by various theoretical calculations as shown, for example, in Fig. 1.13. Line a is for the light quarks, b is for $c\bar{c}$ without the dead-cone effect and c is for $c\bar{c}$ with the dead-cone effect. So, without the dead-cone effect, heavy and light mesons would suffer the same radiative energy loss inside the QGP, but with the dead-cone effect, the radiation energy loss is much smaller for $c\bar{c}$.

This "mass hierarchy" in energy loss can be also seen experimentally. In the following chapter, in Fig. 2.9, the nuclear modification factor R_{AA} for D and B mesons is shown. The heavier B mesons are clearly less suppressed than lighted D mesons, which is in agreement with this theory.

The plot shows dE/dx (GeV/fm) versus E (GeV), with parameters $m = 1.5\,\mathrm{GeV}$, $T = 0.3\,\mathrm{GeV}$, $\alpha_s = 0.3$, $\tau = 1.0$, and curves labeled a, b, c and $c\bar{c}$.

Fig. 1.13: Radiative energy loss of light and heavy quarks in the QGP. Line a is for the light quarks, b is for $c\bar{c}$ without the dead-cone effect and c is for $c\bar{c}$ with the dead-cone effect. Taken from Ref. [22].

Chapter 2

Open heavy-flavor mesons

2.1 Non-photonic electrons and open heavy-flavor mesons

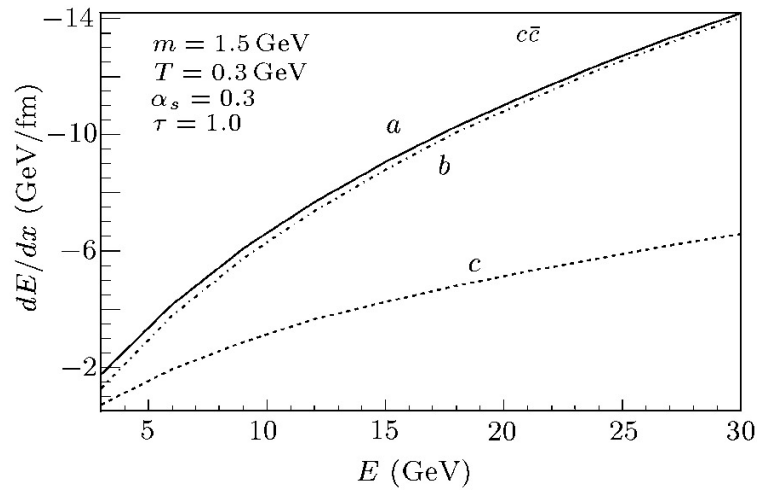Non-photonic electrons (NPE) come from semi-leptonic decays of open heavy-flavor mesons, i.e. D mesons containing c quark and B mesons containing b quark. Most relevant properties of open heavy-flavor mesons are listed in Tab. 2.1. Heavy quarks are good tool for study of the QGP because they are created predominantly in the initial phase of the heavy-ion collisions, during the hard scattering. The QGP fireball is ignited afterwards and the heavy mesons have to pass through the medium. The heavy quarks from the hard scattering strongly interact with the medium and so provide valuable information about the QGP itself.

Meson	M [MeV/c^2]	$c\tau$ [μm]
D^0 ($c\bar{u}$)	$1{,}864.83 \pm 0.05$	$122{,}9 \pm 0{,}4$
D^+ ($c\bar{d}$)	$1{,}869.58 \pm 0.09$	312 ± 2
B^0 ($d\bar{b}$)	$5{,}279.37 \pm 0.15$	456 ± 1
B^+ ($u\bar{b}$)	$5{,}279.62 \pm 0.15$	491 ± 1

Tab. 2.1: Properties of the open heavy-flavor mesons. Their quark composition (left column), mass M (middle column) and mean lifetime τ (right column) are shown. Corresponding antiparticles (not shown) have the same properties (M and τ). Taken from Ref. [23].

The open heavy-flavor mesons have too short lifetime to be detected directly, but have to be reconstructed via their decay products. Mainly two decay channels are used in experiments - the hadronic channel, were all products are hadrons (predominantly lighter mesons), or the semi-leptonic channel, where one or more hadrons, together with leptonic pair, are created. The leptonic pair consists of a charged lepton (electron, positron or muon) and corresponding neutrino.

When using semi-leptonic channel, only electrons are used as they are relatively easy to detect and they are created in relatively large number, because the branching ratio of semi-leptonic decays (containing electron/positron, not muons) of open heavy-flavor is around 10% [23]. The semi-leptonic channel has also advantage compared to the hadronic one that only one decay product has to be reconstructed which is sufficient to obtain information about open heavy-flavor production.

On the other hand, reconstructing just NPE does not provide information about mother particle kinematics, e.g. its momentum. In addition, there is large photonic background consisting of gamma conversion electrons, Dalitz electrons from π^0 and η mesons decay and electron-positron

pairs from decay of J/ψ. Also hadrons, mainly charged pions, which were misidentified contribute to the background. Correct and efficient subtraction of this background is the main challenge in NPE analysis. One way of obtaining the NPE spectrum is to reconstruct the background first and then subtract it from the inclusive electron spectrum. This method is useable when combined NPE spectrum from D and B mesons decay is required, but it can not provide direct information about D and B mesons separately.
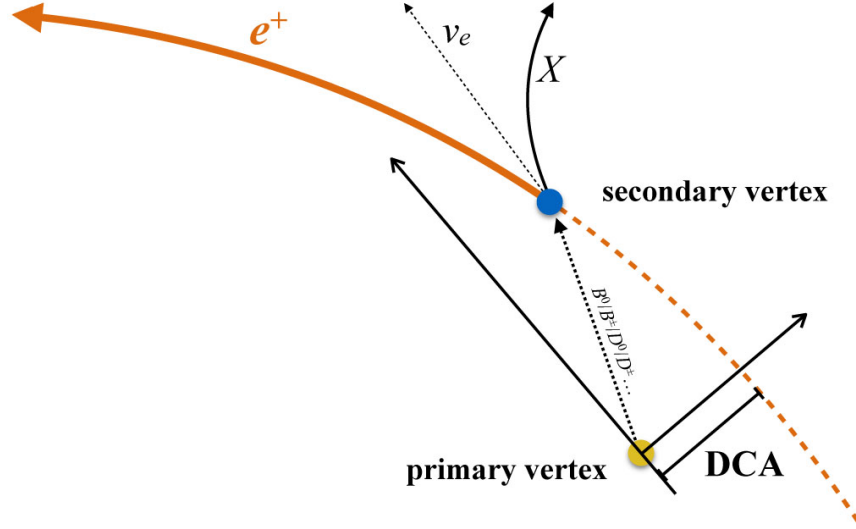

Fig. 2.1: Scheme demonstrating the DCA (distance of closest approach to the primary vertex). The open heavy-flavor mesons decay in distance from the primary vertex due to their relatively long lifetime. Therefore, the elongated track of the electron or positron does not cross the primary vertex. The shortest distance between this track and the primary vertex is denoted DCA. The X in this figure represents a hadron. Taken from Ref. [24].

For that reason, another method of NPE measurement was developed which uses the fact that B mesons have significantly longer lifetime and path-length than D mesons (see Tab. 2.1). When a detector with good primary and secondary vertex position resolution is available, it is possible to tell apart B and D mesons by measurement of the distance of closest approach to the primary vertex (denoted DCA, or alternatively d_0), which is shortest distance between the reconstructed primary vertex and track of one of the decay products, in this case electron/positron, usually measured in plane transverse to the beam axis (then denoted DCA_{xy}), as shown in Fig. 2.1.

Unfortunately, the NPE analysis is not that straightforward as it may appear from description above. Measurement does not provide us specific values of the DCA for different particle species. Instead, the DCA has form of a distribution which tells us how many particles, in this case electrons and positrons, have specific DCA. As will be shown in the proceeding sections, majority of electrons and positrons have DCA $= 0$ μm and significant number of electrons/poistrons is observed for DCA up to approximately 1,000 μm. The required information about production of open heavy-flavor mesons has to be extracted from such DCA distribution for all electron/positrion candidates, i.e. inclusive electron DCA spectrum, which contains also contamination by photonic electrons and hadrons. More detailed description of NPE analysis using the DCA is in sections 2.2.1 and 2.2.3.

2.2   Non-photonic electrons measurement at the RHIC and the LHC

To fully understand the production of D and B mesons, it is crucial to study different colliding systems. The p+p collision are good check if our theoretical prediction works. So far, the data are with good agreement with FONLL (Fixed Order plus Next-to-Leading-Log) calculations. The p+A or d+A collisions provide information about the cold nuclear matter effects. As will be shown in this section, the results are again with reasonable agreement with theoretical calculations. Possibly the most challenging is description of the A+A data. Contemporary models do not describe the experimental too well. The models usually work only for very specific conditions, e.g. for certain particle species or only in given p_T range. Comparison of results from several experiments and colliders can help with description of D and B production in A+A collisions.

Therefore a selection of NPE results, for variety of colliding systems, is presented in this section. First subsection summarises data measured by ALICE experiment at the LHC, the second one shows results by PHENIX experiment at the RHIC and the last one describes results obtained by STAR experiment at the RHIC.

2.2.1   ALICE experiment results
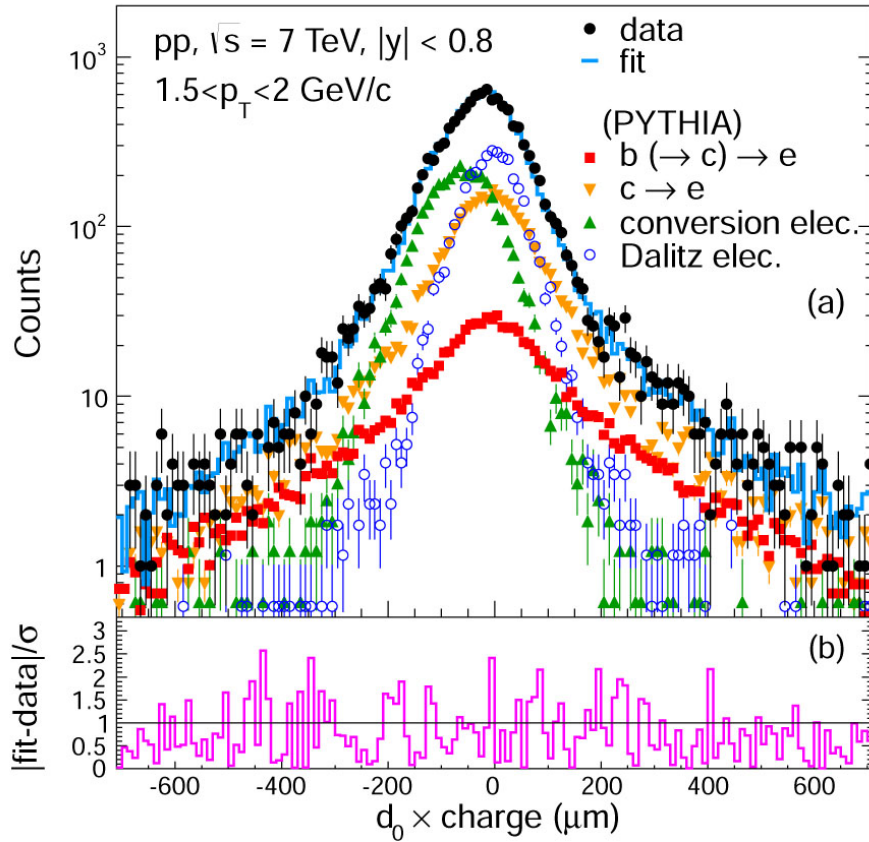
Fig. 2.2: (a) DCA (d_0) distribution measured by ALICE. Black points represent measured inclusive electrons, the other colored points are PYTHIA simulated distributions of individual electron sources (see label in the plot). The blue line is fit of the data and was obtained as a sum of the simulated distributions, where the normalisation of individual components was the free parameters of the fit. (b) Comparison of data and fit. Taken from Ref. [25].

ALICE (A Large Ion Collider Experiment) is experiment at the LHC dedicated primarily to study of heavy-ion (Pb+Pb) collisions, but it also takes reference data from proton-proton collisions and p+Pb collisions. NPE measurement was performed for all of these colliding systems at ALICE where both above described analysis methods were used (background subtraction and DCA).

The DCA method was used for example in Ref. [25] for proton-proton collisions at $\sqrt{s} = 7\,\mathrm{TeV}$. The basic steps of the analysis are as follows: In first step the inclusive electrons DCA spectrum was obtained which was than fitted by sum of histograms from simulation containing information about individual contributions to the inclusive electron spectrum. The fit histograms were obtained from PYTHIA simulation and the normalisation of individual components was used as the free parameters of the fit. The DCA distribution, the simulated components and the fit are plotted in Fig. 2.2.
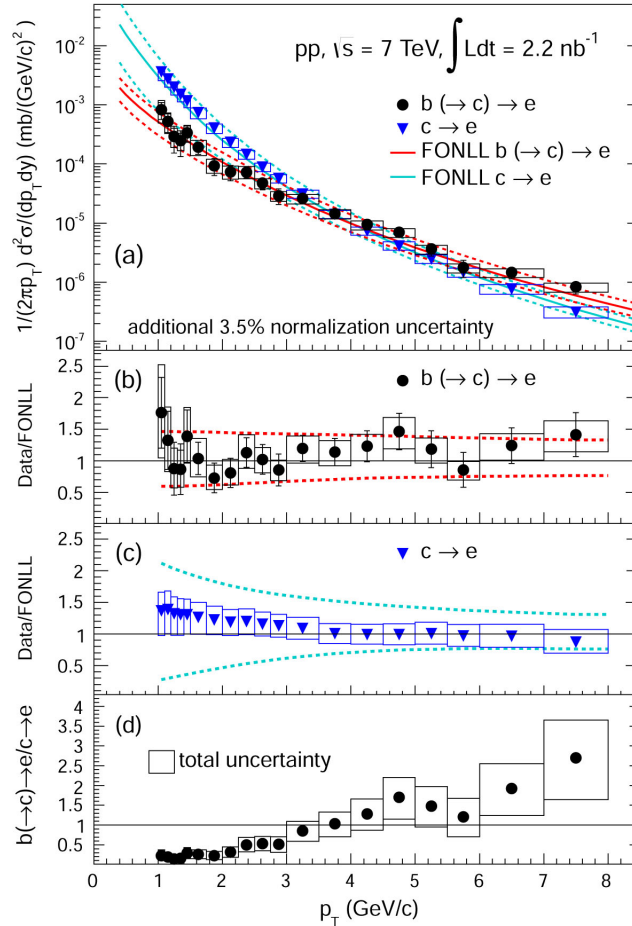
Fig. 2.3: (a) NPE cross-section as a function of p_T for proton-proton collisions at $\sqrt{s} = 7$ TeV measured by ALICE. The black circles represent signal from B mesons decay, the blue triangles represent signal from D mesons decay. The colored lines are prediction by FONLL model. (b) Comparison of data and model for B mesons decay. (c) Comparison of data and model for D mesons decay. (d) Comparison of cross-sections from B mesons and D mesons decay. Taken from Ref. [25].

The fit contains information about ratio of the inclusive electron spectrum components which allows to obtain spectrum of required component, in this case NPE from c and b quarks. Spectrum of NPE from decay of D and B mesons is in Fig. 2.3 where comparison with FONLL model is

also provided. The obtained result is with good agreement with the model, so the DCA method
seems to give correct results.

   If the same procedure is applied to different colliding system, it is possible to compare it to
the proton-proton result. As an example, measurement of nuclear modification factor R_{pPb} is
presented[1]. The R_{pPb} of NPE from decay of c and b combined as a function of p_T can be seen in
Fig. 2.4. In this case, p+Pb at $\sqrt{s_{NN}} = 5.02$ TeV data was compared to the proton-proton data.
This result suggest that there is no significant suppression or enhancement in p+Pb compared to
proton-proton system (within errors), i.e. there is no QGP present in p+Pb collisions.
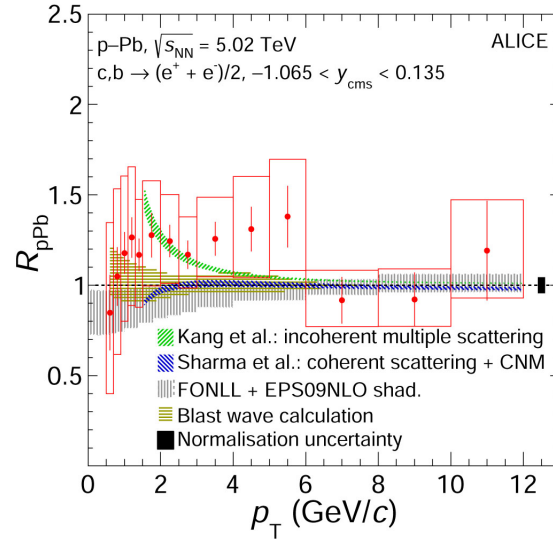
Fig. 2.4: Nuclear modification factor R_{pPb} of NPE from decay of c and b combined as a function of
p_T for p+Pb collisions at $\sqrt{s_{NN}} = 5.02$ TeV measured by ALICE. Several models are also plotted
for comparison. Taken from Ref. [26].
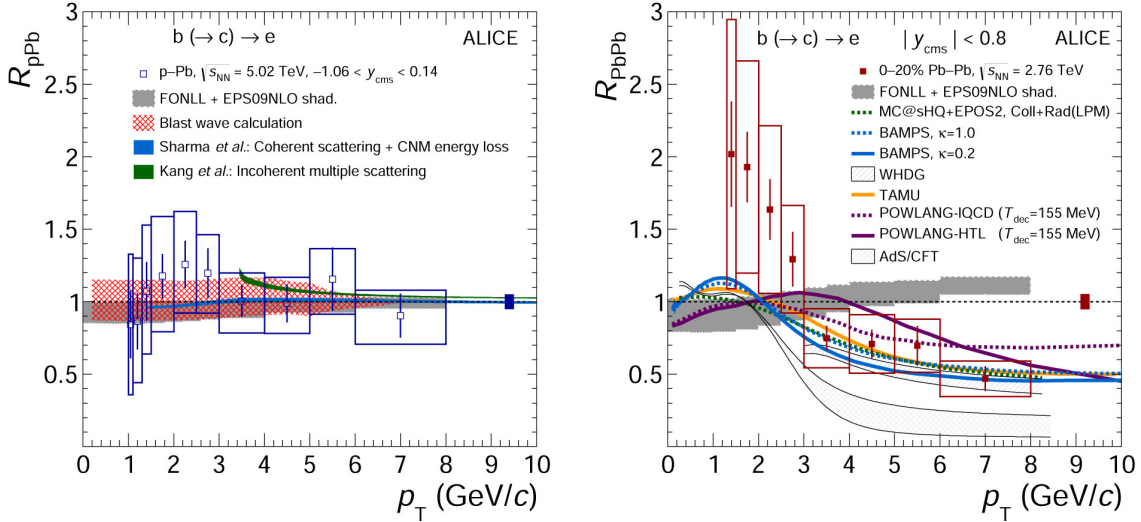
Fig. 2.5: Nuclear modification factor R_{pPb} and R_{AA} of NPE from decay of b as a function of
p_T for p+Pb collisions at $\sqrt{s_{NN}} = 5.02$ TeV and Pb+Pb central collisions at $\sqrt{s_{NN}} = 2.76$ TeV
measured by ALICE. Several models are also plotted for comparison. Taken from Ref. [27].

---

[1]The R_{pPb} compares p+Pb collisions to the proton-proton collisions in the same way as the R_{AA} compares
heavy-ion collisions to the proton-proton collisions.

The ALICE experiment also measured the R_{pPb} for p+Pb collisions at $\sqrt{s_{NN}} = 5.02$ TeV and R_{PbPb} for Pb+Pb at $\sqrt{s_{NN}} = 2.76$ TeV of the NPE just from decay of b using the DCA method. The result of this measurement can be seen in Fig. 2.5. The R_{pPb}, as in previous example, is consistent with unity, i.e. no suppression is observed. In case of R_{PbPb}, on the other hand, a suppression can be seen for $p_T > 3$ GeV/c.

2.2.2 PHENIX experiment results

PHENIX experiment has also performed a NPE measurement. As an example, an invariant yield of NPE is presented in Fig. 2.6. The grey circles represent PHENIX analysis of data taken in the year 2002, where the NPE spectrum was obtained using the background subtraction method [28]. The colored lines are re-folded NPE spectra from D and B mesons decay [29]. Combination of data from Run4 (year 2004) and Run11 (year 2011) were used for the unfolding. The Run4 data were analysed using background subtraction method, the Run11 data were analysed using the DCA method. As can be seen in panel (b) of Fig. 2.6 the measured and re-folded data are in agreement with each other. The refolded data is compared to the STAR experiment preliminary results shown in Fig. 2.8.
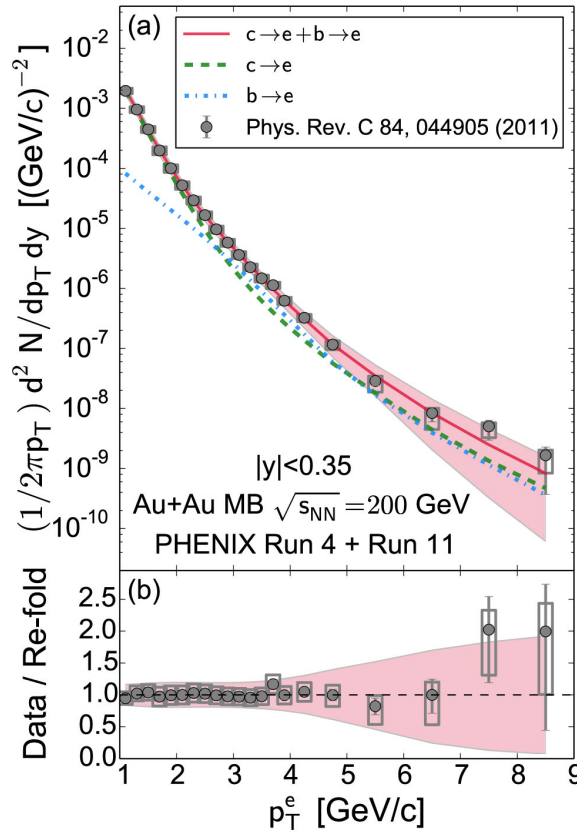
Fig. 2.6: (a) Invariant yield of NPE as a function of p_T for Au+Au collisions at $\sqrt{s_{NN}} = 200$ GeV measured by PHENIX (grey circles, [28]) and re-folded NPE spectra from D and B mesons decay (colored lines). (b) Comparison of data and re-folded spectrum. Taken from Ref. [29].

2.2.3 STAR experiment results

The NPE analysis in Au+Au collisions at $\sqrt{s_{NN}} = 200$ GeV using the DCA method is in progress at the STAR experiment. The recent, preliminary, results from analysis of Run14 data are pre-

sented in this section. The basic approach of the analysis is the same as described in section 2.2.1 about ALICE NPE results.
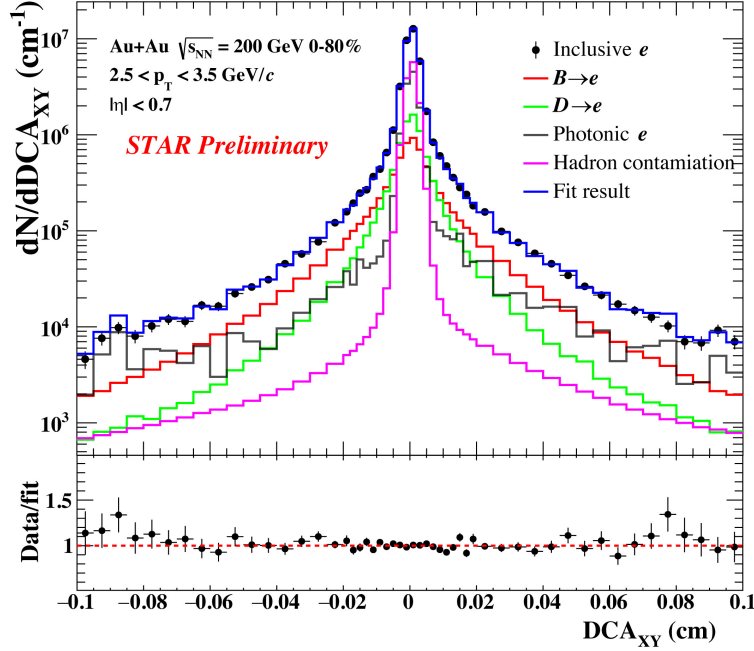
Fig. 2.7: DCA_{xy} distribution of NPE measured by STAR experiment. Black points are the data for inclusive electrons in Au+Au collisions at $\sqrt{s_{NN}} = 200\,\text{GeV}$, the histograms for $B \to e$, $D \to e$ and Photonic e are from simulation, the histogram for Hadron contamination is from data. The Fit result histogram is sum of these four histograms fitted to the data points. The comparison of the data and the fit is shown in the bottom panel. Taken from Ref. [30].

The first step is fitting the inclusive electrons DCA_{xy} distribution as shown in Fig. 2.7. The histogram used for fitting consists of four parts. The fist is the contribution from semi-leptonic decay of B and D mesons which comes from EvtGen+data-driven fast simulation. The second is the photonic background which is obtained from data and HIJING simulation. The last one is hadronic background which is taken from data. The normalisation of individual components was used as free parameters of the fit.

The result of the fit is ratio of the NPE coming from decay of the B mesons and all NPE. Such fit was performed in several different p_T bins and the ratios were plotted as a function of p_T as shown in Fig. 2.8. The Au+Au data from STAR are compared to Au+Au data from PHENIX experiment [29] (see also section 2.2.2) and p+p from STAR experiment and FONLL simulation. The STAR results are with reasonable agreement with FONLL and the PHENIX result.

The fit also allows to obtain information about yield of the D and B mesons in Au+Au collisions which can be subsequently compared to yield form p+p collisions using the nuclear modification factor R_{AA}. The R_{AA} as a function of p_T is shown in Fig. 2.9. The D mesons are suppressed in the whole plotted p_T region whereas B mesons do not seem to be suppressed at STAR experiment. This provides us with interesting comparison with the ALICE experiment data (recall Fig. 2.5), where B suppression was observed.

All STAR results presented above were obtained using the DCA method, i.e. with help of the HFT (see next chapter). The STAR measured the NPE also before the HFT was installed into the STAR detector. A measurement of NPE R_{AA} at the STAR experiment without the HFT is presented in Fig. 2.10.
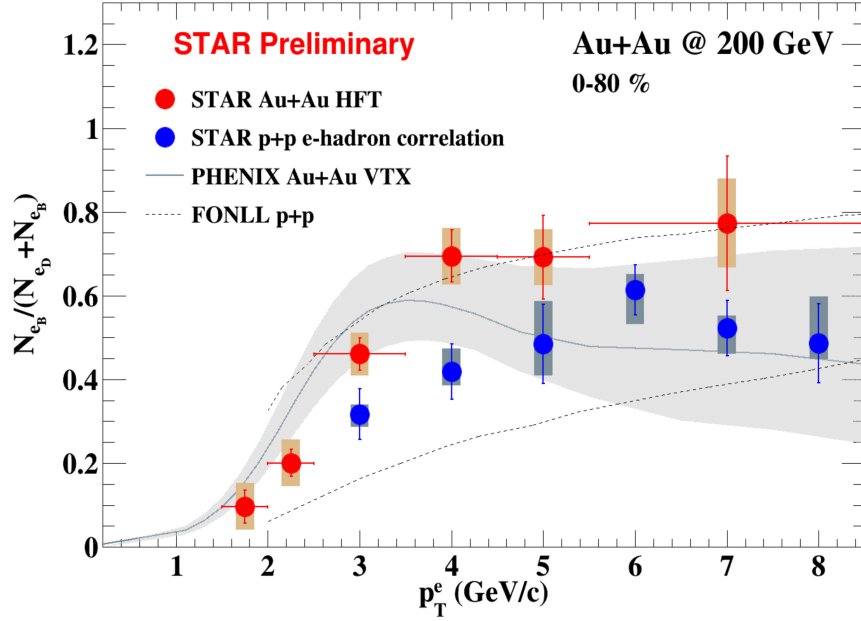
Fig. 2.8: Fraction of NPE coming from decay of B mesons (N_{e_B}) and total NPE yield $(N_{e_D} + N_{e_B})$ as a function of p_T. Red points are Au+Au data obtained by DCA method by STAR, the blue points are p+p data obtained from e-hadron correlation, the solid line with shaded area is result by PHENIX experiment [29] for Au+AU and the dashed line is from FONLL for p+p. Taken from Ref. [30].
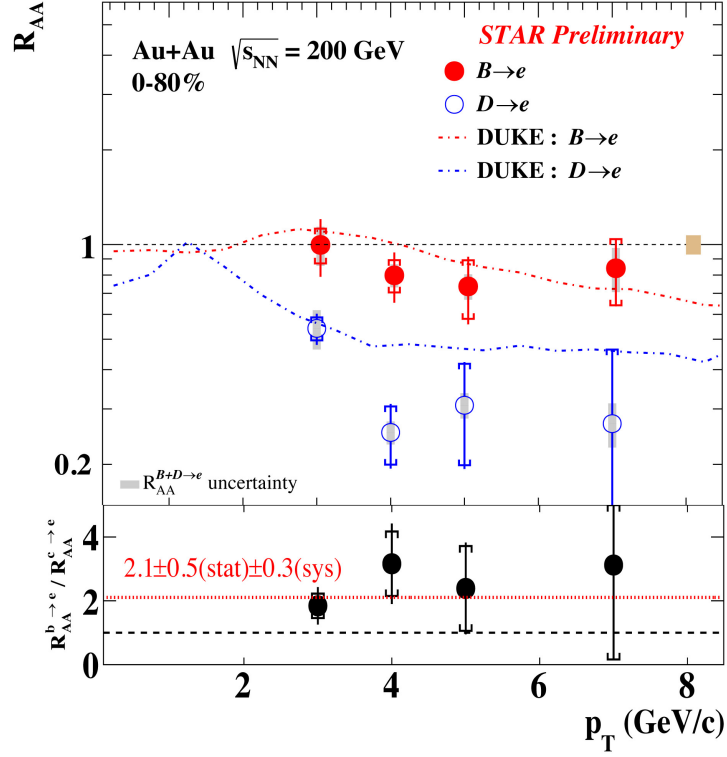
Fig. 2.9: Nuclear modification factor R_{AA} as a function of p_T for NPE form decay of D mesons (blue points) and B mesons (red points). Ratio of R_{AA} from B and D mesons is plotted in the bottom panel. Taken from Ref. [30].
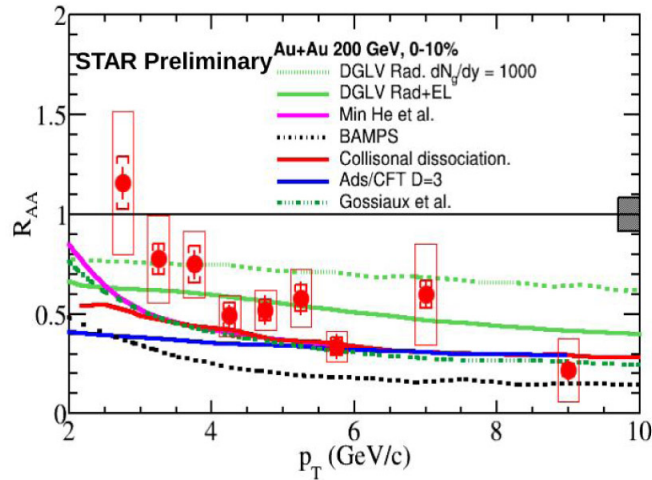
Fig. 2.10: Nuclear modification factor R_{AA} as a function of p_T for NPE measured by the STAR experiment without the HFT. Taken from Ref. [31].

Chapter 3

The STAR experiment

The STAR (Solenoidal Tracker At RHIC) experiment is located in Brookhaven National Laboratory (BNL) on Long Island, New York, USA. It is currently the only experiment at Relativistic Heavy-Ion Collider (RHIC) still taking data. The primary purpose of the STAR is study of the QGP in ultra-relativistic heavy-ion collisions and spin structure of the proton using proton-proton collisions. STAR detector is, for that reason, equipped with number of advanced sub-detectors which allow precise reconstruction and identification of particles created in such collisions.

A brief description of the RHIC and the STAR detector is provided in following two sections. The first is about the RHIC accelerator complex and the second is about STAR sub-detectors important for the NPE study.

3.1 The BNL accelerator complex

3.1.1 Accelerator chain

The particles used for collisions at the RHIC have to be preaccelerated before they are injected to the RHIC itself. Path of (heavy) ions from the source to the RHIC is described in this section. A scheme of the BNL accelerator complex is shown in Fig. 3.2.

The ions start their journey in a laser ion source called LION which is placed in building 930 (see Fig. 3.2). A high-power pulsed laser provides a laser beam which hits a target, e.g. gold plate, which creates +1 ions of desired species. LION is able to produce large variety of ions this way because nearly any solid-state material can be placed into the LION target chamber. In addition, the LION can quickly switch between different targets at frequency of 1 Hz [32] which is beneficial predominantly to NASA Space Radiation Laboratory in BNL studying galactic cosmic radiation. The RHIC uses LION for Au beam creation since June 2014 [32] as it can provide the same output beam intensity as the previous ion source, the Hollow Cathode Ion Source (HCIS). The HCIS used glow discharge in gas to produce the ions [33], which meant that the ions extracted from the HCIS were contaminated by ions of the gas. This behavior is not present while using LION which is its another big advantage.

The +1 ions from the LION are transferred to the Electron Beam Ion Source (EBIS). Scheme of LION and EBIS is shown in Fig. 3.1. Inside the EBIS, the ions are ionised even more using electron beam. In case of ^{197}Au, the EBIS produces short pulses ($\leq 40\,\mu s$) of $3.4 \cdot 10^9$ Au^{32+} ions [34]. The energy of the ions when leaving EBIS is 17 keV/u (energy per one nucleon) [35].

Before entering the Booster Synchrotron, the ions are first accelerated from 17 keV/u to 0.3 MeV/u by the RFQ (Radio Frequency Quardupole) accelerator and then from 0.3 MeV/u to 2.0 MeV/u by Inter-digital H-mode drift tube linac [36]. The Booster Synchrotron then accelerates the ions to 95 MeV/u and forms them into 24 bunches which are subsequently stripped to Au^{77} and injected into the Alternating Gradient Synchrotron (AGS). There they are rebunched into 4 bunches and accelerated to 10.8 GeV/u, then they are stripped to final Au^{79} and transferred into
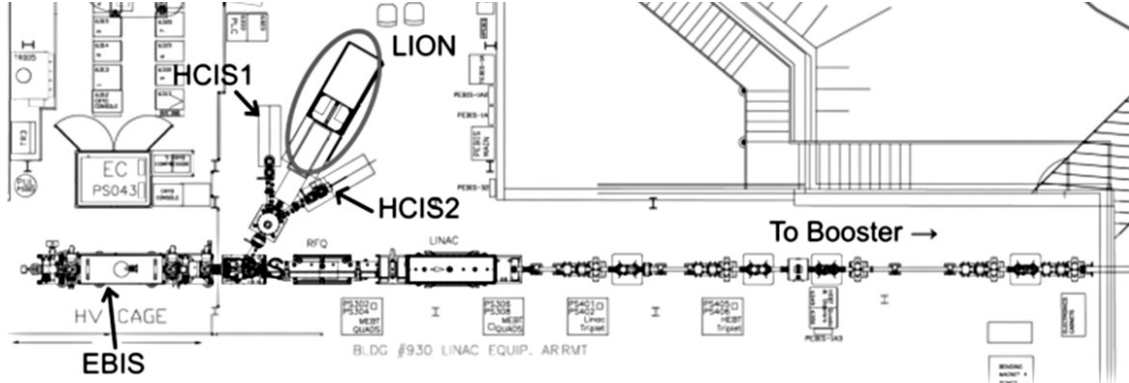
Fig. 3.1: First stage of RHIC heavy-ions accelerator chain. The LION is the Laser Ion Source, EBIS is Electron Beam Ion Source, RQF is Radio-Frequency Quadrupole accelerator and LINIAC is the Inter-digital H-mode drift tube linear accelerator. The HCIS1 & 2 are Hollow Cathode Ion Sources. Taken from Ref. [32].

the RHIC [37]. For Au ions, filling the RHIC is complete when there are 112 bunches stored in each of the RHIC rings [38]. The maximum energy for Au ions in RHIC is 100 GeV/u per beam which allows perform collisions at $\sqrt{s_{NN}} = 200\,\mathrm{GeV/u}$ (energy per nucleon pair).
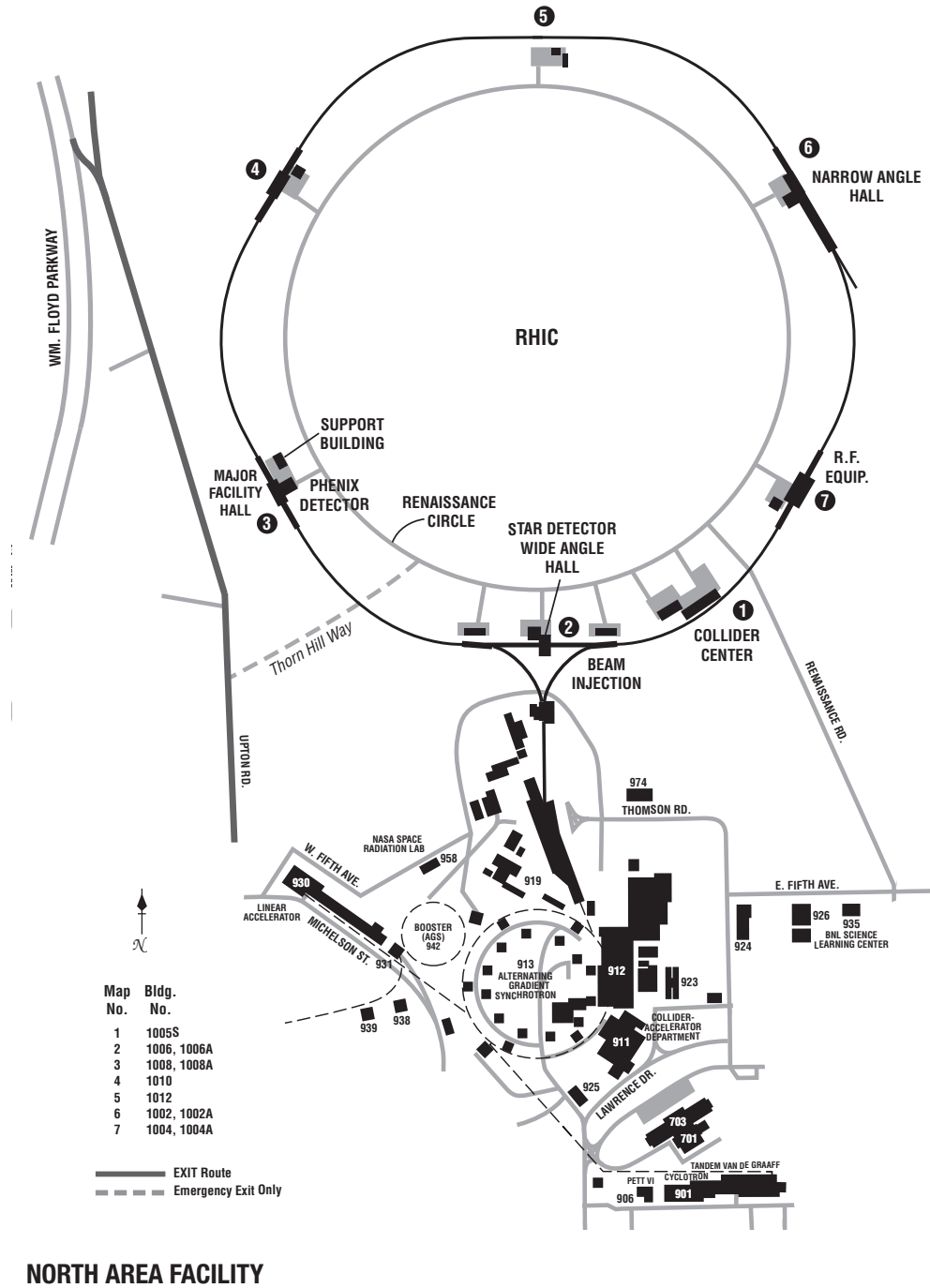
Fig. 3.2: Schematic plan of the BNL accelerator complex. All accelerated particles are first created and preaccelerated in building 930, then they are injected to the Booster (942), next they enter the AGS (913) and finally they are moved to the RHIC. For more detailed description see text. Taken from Ref. [39].

3.1.2 Relativistic Heavy-Ion Collider

Simple scheme of the RHIC is shown in Fig. 3.2. It consist of two concentric synchrotrons with counter-rotating beams[1]. To put thing in perspective, the RHIC has circumference of 3,833.845 m [38]. The collisions are possible at six intersection regions (IR) which are displaced equidistantly around the RHIC. Four of those IR were actually used for experimental measurements.

The STAR experiment, which is located at 6 o'clock of the RHIC[2] (number 2 in Fig. 3.2, is the only experiment still taking data. The PHENIX (Pioneering High Energy Nuclear Interaction eXperiment) was located at 8 o'clock of the RHIC (no. 3 in Fig. 3.2) and it stopped data taking during the year 2016. The remaining two experiments, the PHOBOS at 10 o'clock and BRAHMS (Broad RAnge Hadron Magnetic Spectrometer) at 2 o'clock (no. 4 and 6 respectively in Fig. 3.2), stopped with measurement during the year 2006.

The particles to be studied are injected from the AGS to the RHIC at 6 o'clock position. The two RHIC synchrotrons are filled step-by-step, i.e. one at a time. After the filling of both rings is complete, the stored particles are accelerated to desired energy by four RF (Radio Frequency) cavities (two per beam) with operating frequency of 28.15 MHz. The accelerated beams are then preserved using RHIC storage RF cavities with operating frequency of 197 MHz. There are three such cavities at each ring with additional four cavities common for both rings which gives total of 10 storage RF cavities at the RHIC [38].

The beams are kept inside the RHIC by 888 magnets from which 396 are dipoles and 492 are quadrupoles. Furthermore, the magnets can be divided into two classes. There are so called arc magnets (dipoles and quadrupoles) whose primary purpose is to keep the beam on the circular orbit[3]. Then there are the insertion magnets (again dipoles and quardupoles) which are placed in front of and behind each IR. Their function is to prepare both beams for, so called, bunch crossing at the IR.
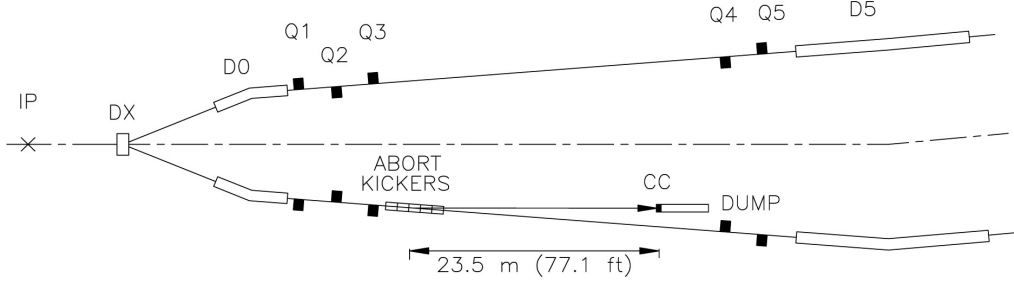
Fig. 3.3: Scheme showing position of beam dump (denoted DUMP) with respect to the nearest IP (not in scale). Magnets within 90 m from the IP are also shown (D - dipole, Q - quardupole). Taken from Ref. [38].

Run	N_{bunch}	$N_{\text{ions/bunch}}$	$L_{\text{store}}^{(avg)}$ [cm^{-2}s^{-1}]	$\mathcal{L}_{\text{week}}$ [nb^{-1}]	$\mathcal{L}_{\text{STAR}}$ [nb^{-1}]
Run14	111	$1.6 \cdot 10^9$	$50 \cdot 10^{26}$	2.2	20.7
Run16	111	$2.0 \cdot 10^9$	$87 \cdot 10^{26}$	3.0	21.9

Tab. 3.1: Selection of performance figures of the RHIC for Run14 and Run16 Au+Au collisions at $\sqrt{s_{NN}} = 200$ GeV. The N_{bunch} is number of bunches per ring, $N_{\text{ions/bunch}}$ is number of ions per bunch, $L_{\text{store}}^{(avg)}$ is average luminosity per store, $\mathcal{L}_{\text{week}}$ is integrated luminosity per week and $\mathcal{L}_{\text{STAR}}$ is total integrated luminosity delivered to the STAR experiment. Taken from Ref. [40].

---

[1] The beams at the RHIC are referred as the blue beam and the yellow beam.
[2] The position of individual IR is denoted as if they were on a clock-face.
[3] The orbit is in fact polygonal and not circular which is given by synchrotron design.

The beam quality is decreasing over time due to the collisions so, at some point, it is not suitable for physics measurement any more. At that moment the beam is disposed of in so called beam dump. This system consist of two main components. The first one is a kicker magnet which deflects the beam from its stable orbit into a dump core, the second component. Simplified scheme showing position of the beam dump with respect to the nearest IR and RHIC magnets is shown in Fig. 3.3. As the dump core is relatively close to the kicker magnet due to limited space available inside the RHIC tunnel, the dump core had to be designed so that it can withstand the stress induced by the dumped beam. Extensive study was carried out while designing the core [41]. The resistance of individual materials used in the core and close proximity of the Q4 quadrupole (see Fig. 3.3) were taken into account. The whole beam is dumped in just one beam revolution (approx. 13 μs) and in case of emergency, the safety system is able to take action and dump the beam within four beam revolutions (approx. 52 μs) [38].

At the end of this section, selection of the RHIC performance for Run14 and Run16 Au+Au collisions at $\sqrt{s_{NN}} = 200$ GeV is summarized in Tab. 3.1. The RHIC performance changes every run so Run14 was chosen because its analysis was done for this thesis and Run16 was chosen as it is the most recent Au+Au collisions at $\sqrt{s_{NN}} = 200$ GeV data-set.

3.2 STAR detector

The STAR detector is a complex system of multiple sub-detectors which are surrounding the RHIC 6 o'clock IR. The whole system is closed inside a large solenoidal magnet that provides 0.5 T magnetic field parallel to the beam axis [42]. A cross section of the STAR detector is shown in Fig. 3.4.
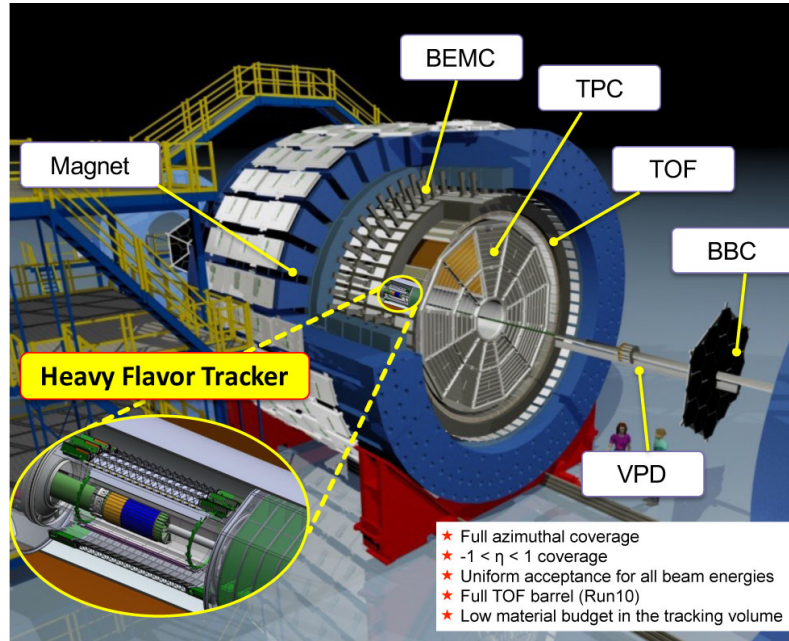
Fig. 3.4: Scheme of the STAR detector and its sub-detectors. For NPE study following detectors are used: the Heavy Flavor Tracker (HFT), the Time Projection Chamber (TPC), the Time Of Flight (TOF) detector, the Barrel ElectroMagnetic Calorimeter (BEMC) and the Vertex Position Detector (VPD). The Beam-Beam Counter (BBC) is used for measurements with polarised protons. Taken from Ref. [24].

The sub-detectors relevant for the NPE analysis are the Heavy Flavor Tracker (HFT), the Time Projection Chamber (TPC), the Time Of Flight (TOF) system and the Barrel Electro-Magnetic

Calorimeter (BEMC) with the Shower Maximum Detector (SMD). All these detectors cover full azimuthal angle ϕ and $|\eta| < 1$ in longitudinal direction. Each of them plays important role when detecting and reconstructing electrons. For that reason, a brief description of each sub-detector listed above is provided in following four sections.

3.2.1   Heavy-Flavor Tracker

The HFT is a 4-layer silicon detector dedicated to precise primary and secondary vertex reconstruction which is useful when measuring particles with relatively long lifetime such as the open heavy-flavor mesons. It was installed into the STAR detector in year 2014 when it replaced older Silicon Vertex Tracker (SVT). The firs two layers at 2.5 cm and 8.0 cm from the beam axis are the pixel sensors, the middle layer, the Intermediate Silicon Tracker (IST), is 14.0 cm from the beam and the last layer, the Silicon Strip Detector (SSD), is located 22.0 cm from the beam. A scheme of the HFT is shown in Fig. 3.5.
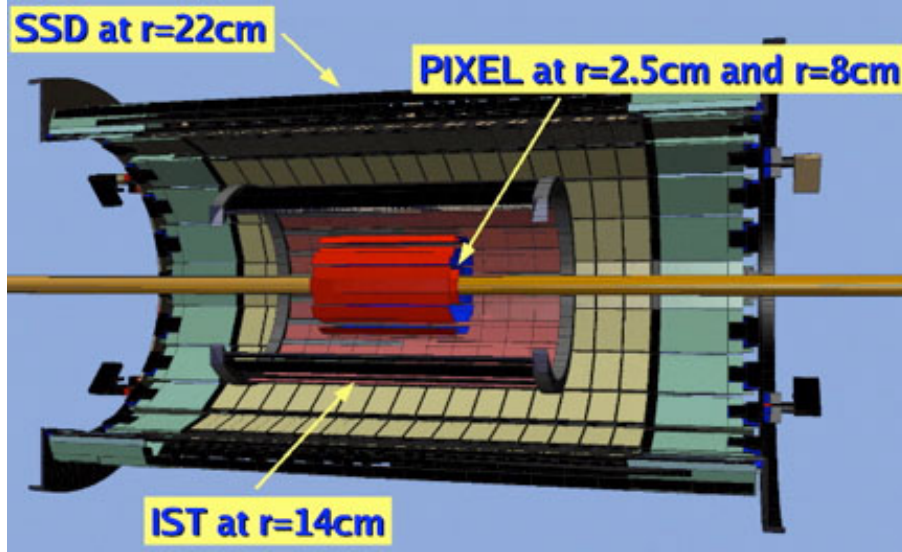
Fig. 3.5: Scheme of the STAR Heavy Flavor Tracker (HFT). The first two layers are silicon pixel detectors (PIXEL), the third layer is the Intermediate Silicon Tracker (IST) and the last layer is the Silicon Strip Detector (SSD). Taken from Ref. [43].

The two PIXEL layers consist of 40 ladders, 10 in inner layer and 30 in outer layer, where each contains 10 CMOS (Complementary Metal-Oxide Semiconductor) detector chips. Each chip is a Monolithic Active Pixel Sensor (MAPS) consisting of 928×960 pixel array with $20.7\ \mu\mathrm{m} \times 20.7\ \mu\mathrm{m}$ pixels. This gives total of 365.352 millions pixels it the whole PIXEL sub-detector. One of main advantages of MAPS used in HFT is their small, so called, material budget, i.e. the sensors are very thin, just 50 μm, which reduces multiple Coulomb scattering in the detector compared to more conventional hybrid pixel sensors. A 3D rendering of the HFT PIXEL is shown in Fig. 3.6.

The IST has 144 silicon sensors held by 24 carbon-fibre ladders, i.e. 864 sensors in total. It is 50 cm long which means total area of approximately 0.4 m^2. The total number of channels from the IST is 110,592. The main purpose of the IST is to improve track reconstruction resolution between the PIXEL and the SSD. Scheme of the IST is shown in Fig. 3.7.

The purpose of the last layer of the HFT, the SSD, is similar to the purpose of the IST with, but it improves the track reconstruction resolution between the IST and the TPC. It has 40 ladders which carry 16 two-sided wafers each, meaning total of 320 wafers. One side of each wafer has 768 strips which gives a total of 491,520 channels from the SSD. The cheme of the SSD is shown in Fig. 3.8. Just to note, the SSD was also part of the older SVT, but the readout electronics was upgraded for the HFT.
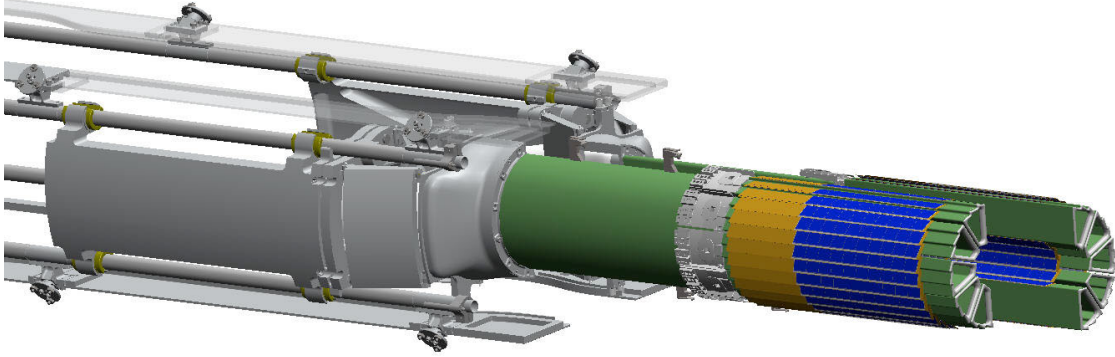
Fig. 3.6: A 3D computer model of the HFT PIXEL sub-detector. The ladders (blue) are mounted on 10 carbon-fibre beams, each carrying 1 inner ladder and 3 outer ladders. The whole support structure of the PIXEL is shown. Taken from Ref. [43].

To put thing into perspective, the values of track reconstruction resolution are listed in Tab. 3.2 and pointing resolution of the STAR HFT as a function of p_T in plane transverse to the beam axis for identified particles is shown in Fig. 3.9.

Part of the track	Resolution
TPC $\rightarrow$ SSD	≈ 1 mm
SSD $\rightarrow$ IST	$\approx 400\,\mu$m
IST $\rightarrow$ PIXEL-2	$\approx 400\,\mu$m
PIXEL-2 $\rightarrow$ PIXEL-1	$\approx 125\,\mu$m
PIXEL-1 $\rightarrow$ vertex	$\approx 40\,\mu$m

Tab. 3.2: Track reconstruction resolution of the HFT together with the TPC. The resolution improves with every layer of the HFT while going from the TPC to the vertex. Here PIXEL-1 and PIXEL-2 denote inner and outer layer of the HFT PIXEL. Taken from Ref. [43].

Finally, it is necessary to note that all facts and values presented in this section are reproduced from Ref. [43]. The HFT was removed from the STAR detector after data taking in the year 2016.
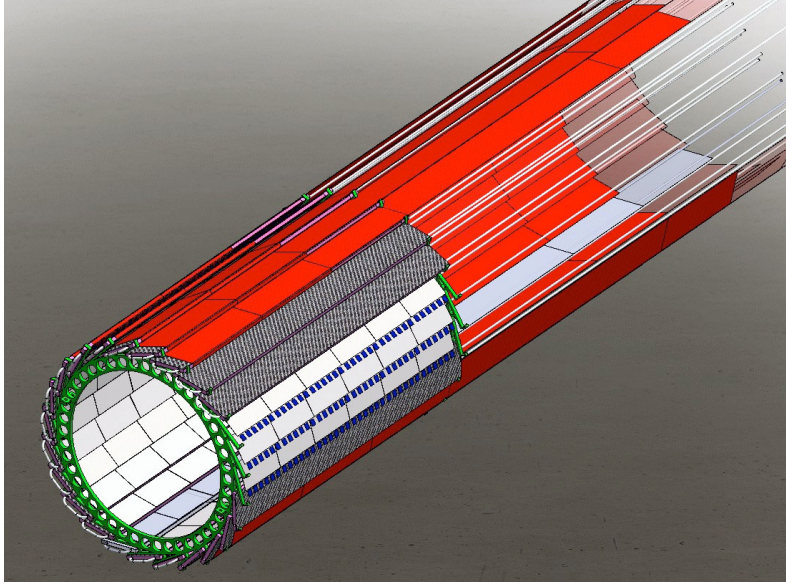
Fig. 3.7: Schematic rendering of the HFT Intermediate Silicon Tracker (IST). Taken from Ref. [43].

Fig. 3.8: Schematic rendering of the HFT Silicon Strip Detector (SSD). Taken from Ref. [43].

Fig. 3.9: Pointing resolution of the STAR HFT as a function of p_T in plane transverse to the beam axis for identified particles. Taken from Ref. [44].

3.2.2   Time Projection Chamber

The TPC is the most important sub-detector in STAR detector. It is responsible for particle identification (PID) and for measuring particle momentum. It is a large gas-filled detector with MWPC (Multi-Wire Proport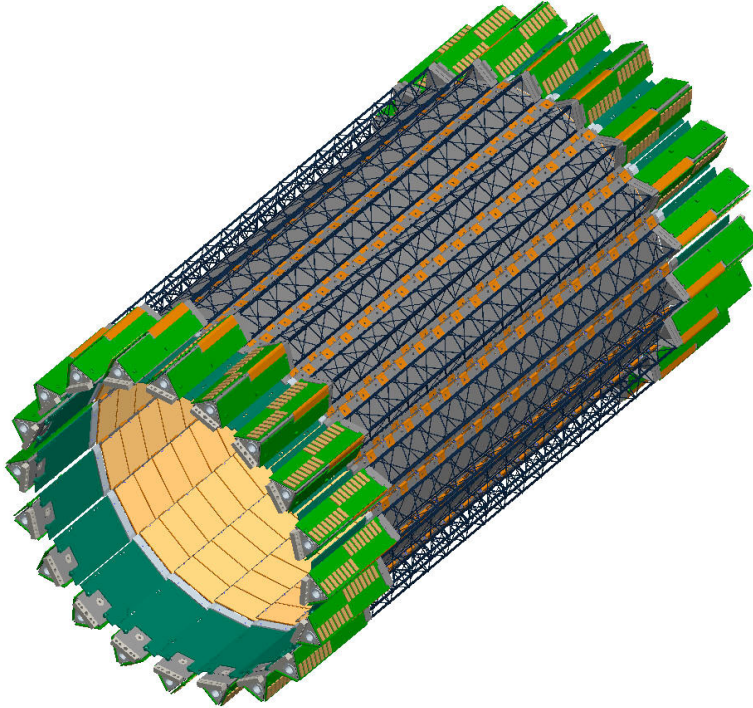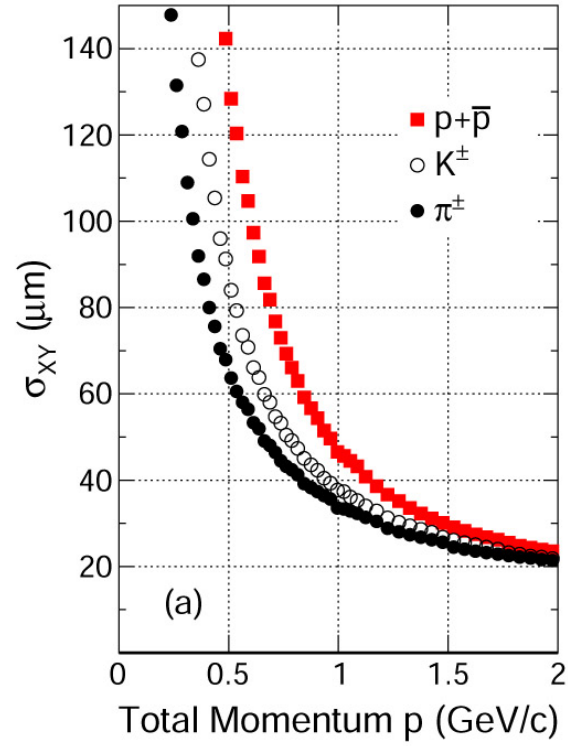ional Counter) readout. Scheme with cross section of the TPC is shown in Fig. 3.10. In the middle of the TPC there is a high voltage (HV) cathode and the MWPC readout sectors are at both ends of the TPC. There is also an inner filed cage on the inner shell of the TPC and outer field cage on the outer shell of the TPC, both placed inside the volume of the TPC. The dimensions of the STAR TPC are: length 4.5 m, inner diameter 1.0 m and outer diameter 4.0 m.
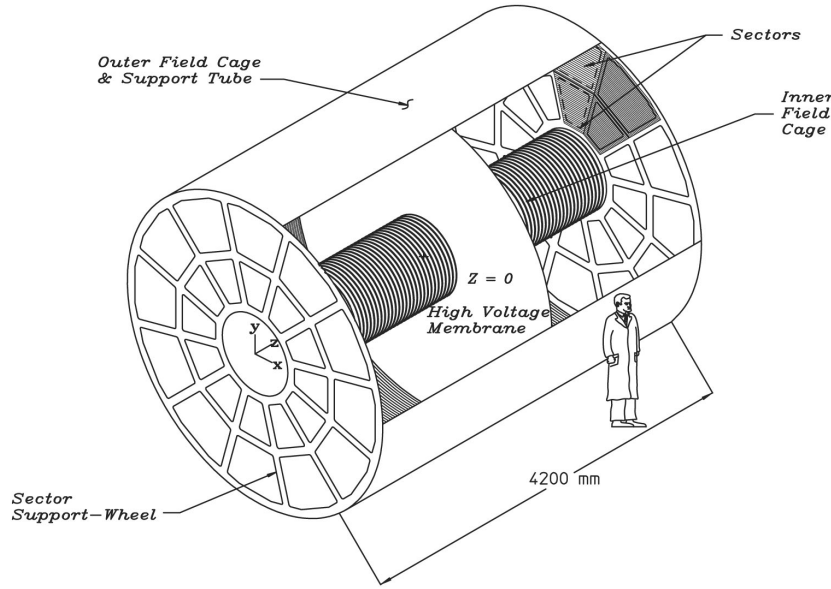
Fig. 3.10: Scheme of the STAR Time Projection Chamber (TPC). Simple description is provided in the scheme. Taken from Ref. [45].

The HV cathode is typically set to value of -28 kV, providing an electric field between the cathode and MWPC sectors of 140 Vcm^{-1}. The field cage (inner and outer) ensures that this field is uniform in the whole TPC volume. Region between the cathode and the MWPC sectors is called a drift volume. When a charged particle passes through the TPC, it leaves there a track of ionised gas. The electrons are subsequently moved towards the MWPC sectors and the ions towards the cathode. No secondary ionisation of the TPC gas in the drift volume occurs.

The amplification and signal readout is done inside the MWPC modules with pad readout. There are total of 12 outer and 12 inner MWPC modules at each side of the TPC (48 modules at both sides of the TPC). Scheme of one outer MWPC module is shown in Fig. 3.13. The electrons entering the MWPC module have to first pass through the gated grid which is a set of wires that allows the electrons to enter the MWPC module only when the experiment electronics gives appropriate command. The electrons continue around the shield grid to the anode grid. The anode wires are set to value of 1,170 V for inner modules and 1,390 V for the outer modules[4]. The electrons are accelerated by the anode wires so that they induce avalanches. The electrons are collected directly by the anode wires and the ions from the avalanches are collected by the shield

---

[4]The actual values can slightly differ during actual data taking. It depends on condition of the TPC MWPC modules.
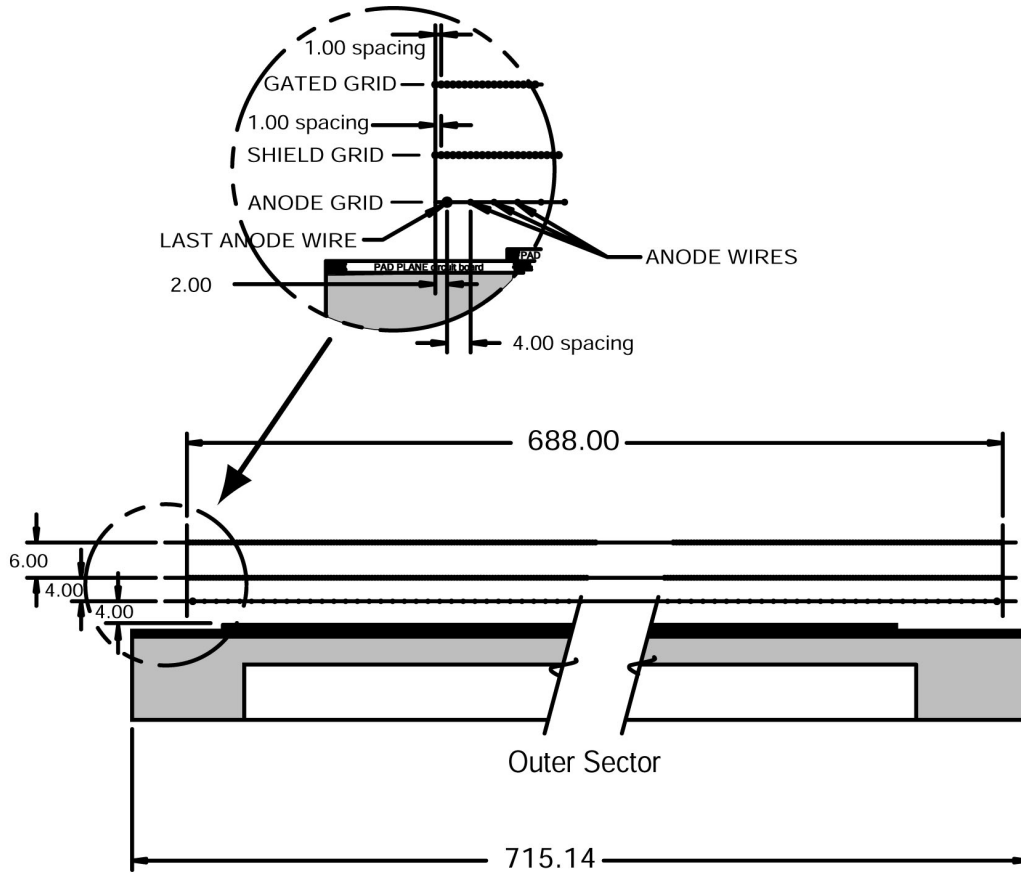
Fig. 3.11: Scheme of the outer MWPC readout panel used in STAR TPC. The dimensions are in milimeters. Taken from Ref. [45].

grid, after they are moved toward it. The signal is collected by the readout pads. The electrons from the avalanches are collected very quickly compared to ions from the avalanche. Thus the ions induce a temporary image charge on the pads which is then transformed into signal.

The TPC gas contains 10% methane and 90% argon (P10 gas) at 2 mbar overpressure. The argon is responsible for the avalanche formation and the methane prevents formation of Geiger discharge because methane molecules effectively absorb UV photons emitted by the accelerated electrons inside the avalanche. In another words, the methane ensures that the MWPC modules work in proportional mode which is necessary for correct PID. The particles are identified based on energy loss in the gas which is possible because the number of electron-ion pairs created by the passing (charged) particle is directly proportional to energy deposited in the TOF gas. The particle momentum is then established based on radius (curvature) of the track detected by the TPC. The tracks of charged particles are curved because of the magnetic field provided by the STAR magnet and because there are 5,692 pads in the whole TPC which allows precise track reconstruction.

An example of PID using the TPC is shown in Fig. 3.12 where energy loss per unit of path length dE/dx is plotted as a function of momentum p for variety of particle species. In this case, it is possible to distinguish e.g. protons from other particles up to $p \approx 1$ GeV/c. On the other hand, telling apart electrons, muons and pions is not possible just from this plot. For that reason, additional detectors are needed to help the TPC with PID. The dE/dx resolution is approx. 8%

Fig. 3.12: Energy loss per unit of path length dE/dx as a function of momentum p for variety of particle species. The measurement was performed with magnetic filed of 0.25 T. Protons can be easily separated from other particles for p up to approx. 1 GeV/c. Taken from Ref. [45].

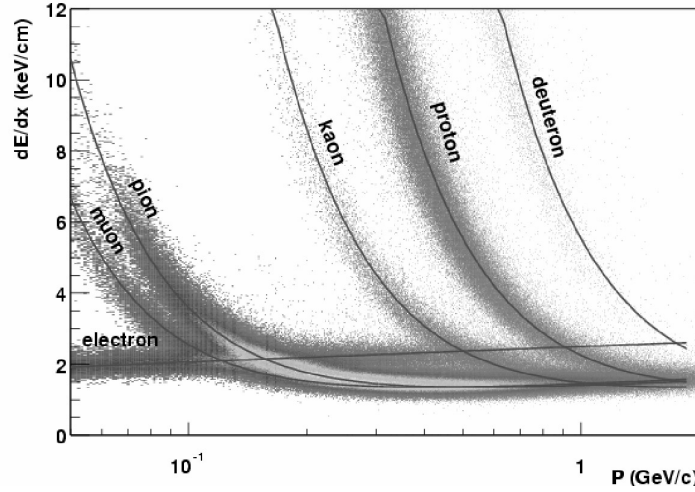if the track of a charged particle is required to have at least 20 hits inside the TPC [46].

All information in this section was taken from Ref. [45], if not stated otherwise.

3.2.3 Time Of Flight detector

The Time Of Flight (TOF) system helps with identification of particles, mainly electrons, with transverse momentum $p_T < 2\,\text{GeV}/c$. The general principle of operation is very simple. The TOF measures speed of particles produced in a collision from time difference Δt of signal in Vertex Position Detector (VPD) and TOF Multi-gap Resistive Plate Chambers (MRPC). There are tow VPD modules placed 5,7 m from IP, one on each side of the STAR detector, very close to the beam pipe at $4.24 < \eta < 5.10$ [47]. The MRPC modules are placed between the TPC and the BEMC covering full $360°$ in azimuthal direction and $|\eta| < 1$ in longitudinal direction (recall Fig. 3.4). For calculation of particle speed $\beta = \frac{v}{c}$ additional information from the TPC about length of the particle track s is required. The final relation for particle speed then reads

$$\frac{1}{\beta} = \frac{c\Delta T}{s}. \tag{3.1}$$

Generally, the main requirement for the TOF system dub-detectors is that they have to be very fast. That is why the combination of the VPD and MRPC was chosen. Scheme of the TOF MRPC module is shown in Fig. 3.13. It consists of 7 glass plates with 0.22 mm spacing. The gaps are filled with mixture of 90% $C_2H_2F_4$, 5% iso-butane and 5% SF_6. The set of plates is "sandwiched" between two graphite electrodes (black in Fig. 3.13) providing voltage of 14 kV. The readout is done using readout pads (red in Fig. 3.13). A charged particle passing through the MRPC ionizes the gas, the created electrons are accelerated by the electric field creating avalanches that are detected by the readout pads.

The VPD is a different type of detector. Each VPD sector contains 19 scintillator detectors with Pb absorber and fast plastic scintillator Eljen EJ-204 which is read out by photo-multiplier tube [47]. It is a very important sub-detector in STAR detector. In addition to TOF system, it serves as one of main triggers and is also used for determination of primary vertex position along the beam axis. A scheme and a photo of the VPD modules is shown in Fig. 3.14.

The TOF system performance is summarized in Fig. 3.15 where particle mass resolution of STAR TOF as a function of particle momentum is shown. For specific values of the time t, momentum p and path length s resolutions see the plot. The particles can be identified only in region
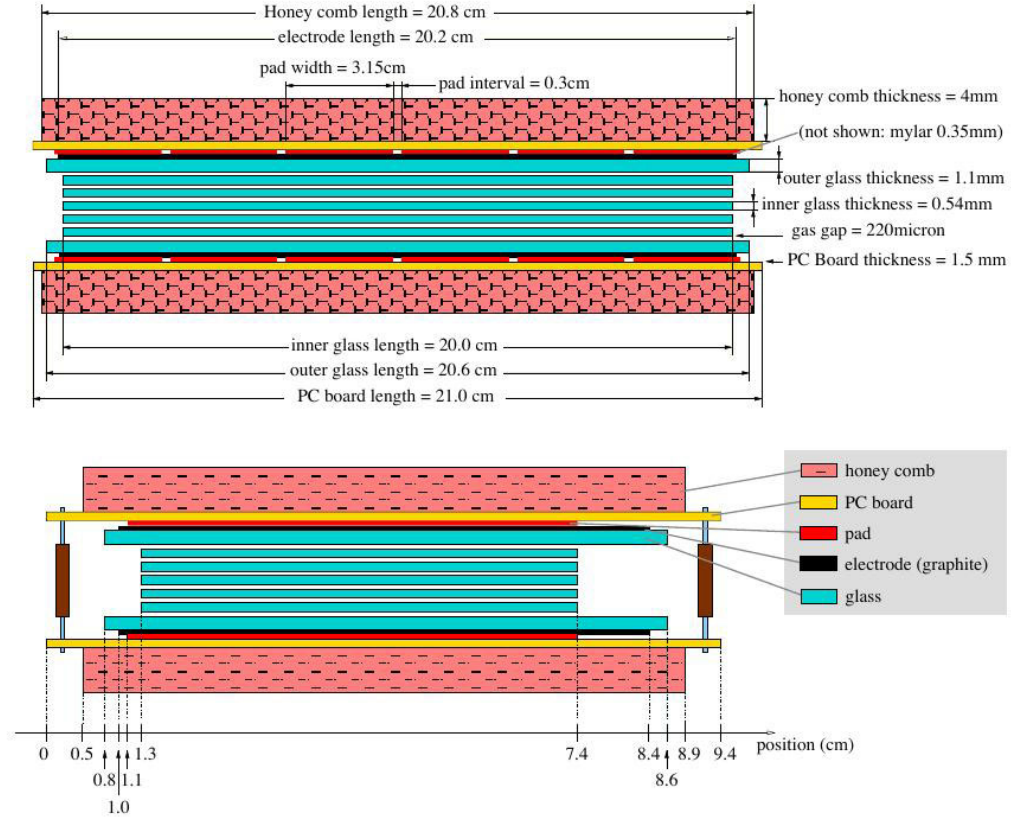
Fig. 3.13: Scheme of the Multi-gap Resistive Plate Chamber (MRPC) used as a part of the STAR TOF system. Description of individual components is provided in the scheme. Taken from Ref. [48].

where the lines are not overlapping. The solid line corresponds to path length at pseudorapidity $\eta \approx 1$ and the dashed line to $\eta \approx 1$.
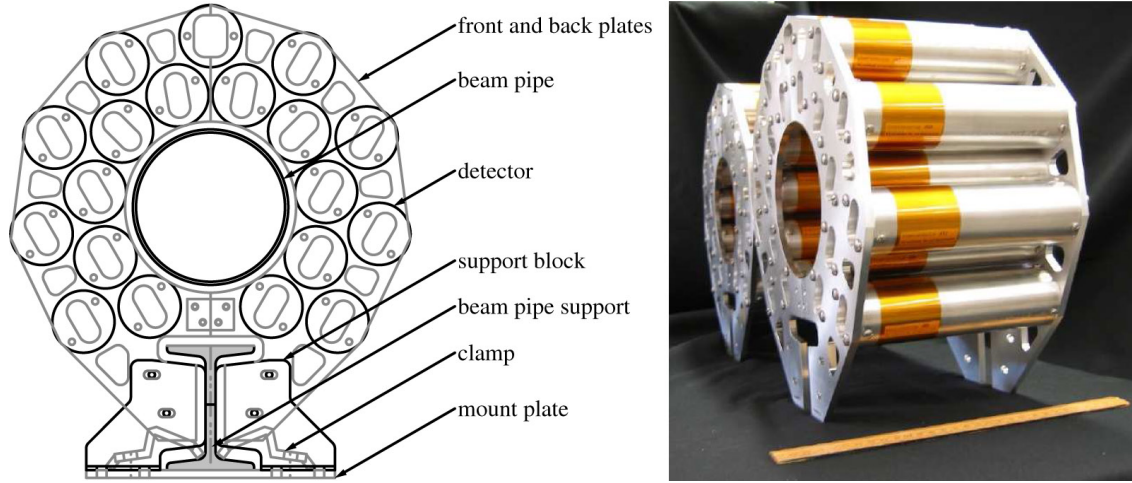
Fig. 3.14: Schematic view (left) and photo (right) of the Vertex Position Detector. The ruler int the photo is 30.48 cm (1 ft) long. Taken from Ref. [47].
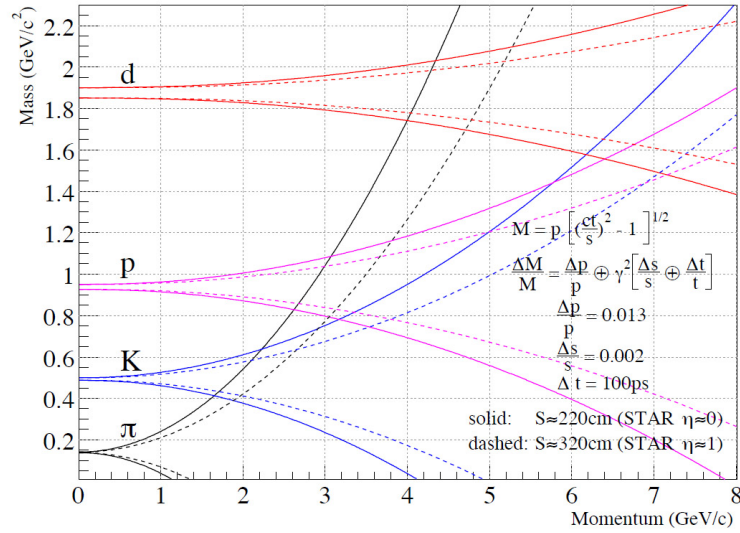
Fig. 3.15: Particle mass resolution of STAR TOF as a function of particle momentum. Taken from Ref. [48].

3.2.4 Barrel Electromagnetic Calorimeter

When measuring particles with transverse momentum $p_T > 2$ GeV, the TOF system can not be used. In that case the Barrel Electro-Magnetic Calorimeter (BEMC) is used instead. The BEMC has the same spatial coverage as the TOF, i.e. $\phi = 360°$ in azimuthal direction and $|\eta| < 1$ in longitudinal direction. The BEMC consists of 120 modules where each covers $\phi = 6°$ in azimuthal direction and $\eta = 1$ in longitudinal direction. Schematic side-view of one BEMC module is shown in Fig. 3.16.
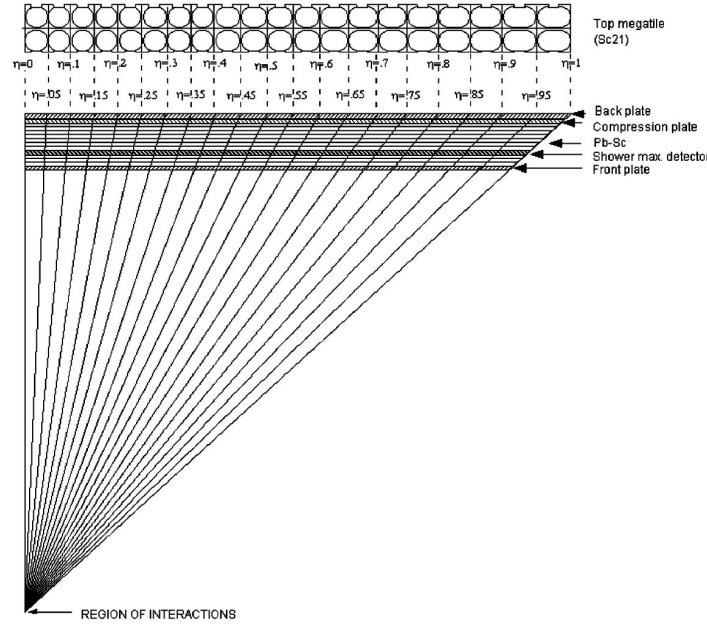
Fig. 3.16: Scheme of the Barrel ElectroMagnetic Calorimeter (BEMC) module layout. Position of the Shower Maximum Detector is also shown. Taken from Ref. [49].

Individual modules contain 40 towers which are aligned in two rows in ϕ, each with 20 towers in η. A single tower contains 20 5 mm thick Pb absorber plates and 21 5 mm thick active scintillating layers. The readout of one box is done by single photo-multiplier tube (PMT). As there are total of 4,800 BEMC towers, there are also 4,800 PMTs which are contained in 60 boxes, each having 80 PMTs inside. Scheme of one BEMC tower is shown in Fig. 3.17.

A charged particle which enters the BEMC is scattered inside the Pb absorber plates and creates shower of charged particles and photons. The shower is then detected by the scintillating plates and PMTs. The PID is done based on how much energy did the particle deposit inside the BEMC. More specifically a quantity $\frac{p}{E_0}$ is measured where p is particle momentum measured by the TPC and E_0 is energy deposited in the BEMC. A light particle, such as electron, will leave most or all of its energy inside the BMEC. A heavy particle, like for example proton, will leave just relatively small fraction of its energy inside the BEMC. Deposited energy E_0 resolution for electrons with energy of 1.5 GeV is approx. 17% and with energy of 3.0 GeV it is approx. 10%.

For better PID, the BEMC is equipped with the Shower Maximum Detector (SMD). The position of the SMD inside the BEMC is shown in Fig. 3.16 and 3.17. It is a proportional counter filled with 90% argon and 10% CO_2. It is designed so that it measures size of the shower induced by incoming particle as shown in Fig. 3.18. This information can help with identification of electrons as showers induced by lighter particles are larger than showers induced by heavier particles.

All information about the BEMC+SMD in this section was taken from Ref. [49].

Fig. 3.17: Scheme of one BEMC + SMD tower and its components. Dimensions are also provided in the scheme. Taken from Ref. [49].

Fig. 3.18: Scheme of the Shower Maximum Detector (SMD). Shape of the signal form the SMD is also shown. [49].

Chapter 4

Non-photonic electrons in Au+Au collisions at $\sqrt{s_{NN}} = 200\,\textbf{GeV}$

Analysis of NPE in Au+Au collisions at $\sqrt{s_{NN}} = 200\,\text{GeV}$ measured by the STAR experiment is presented in this chapter. The chapte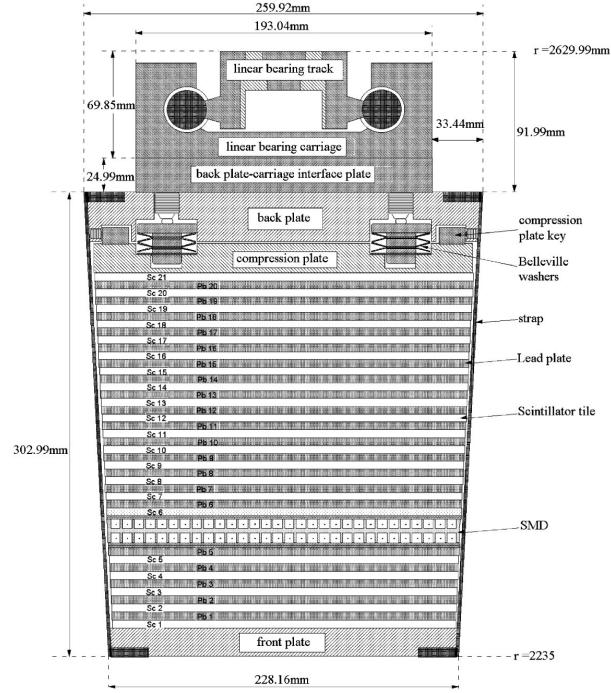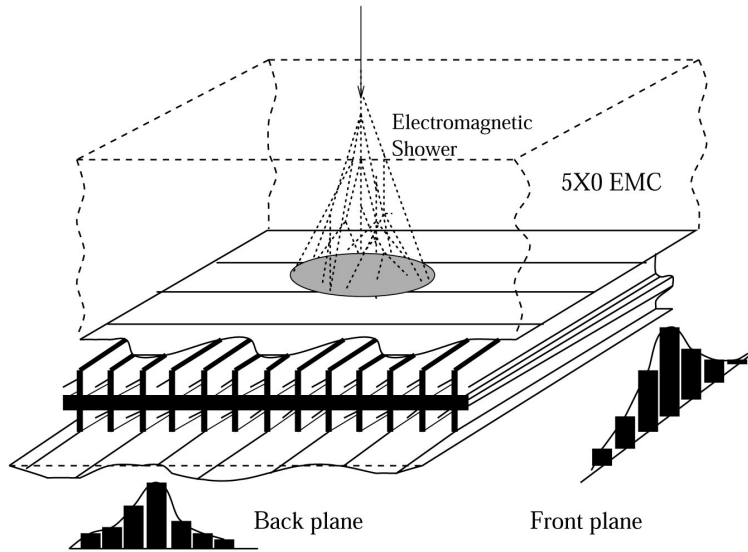r is divided into two sections where the first summarises information about used data sample and the second is dedicated to description of individual steps of the NPE analysis.

4.1   Experimental data

For this analysis the Run14 (year 2014) data of Au+Au collisions at $\sqrt{s_{NN}} = 200\,\text{GeV}$ measured by the STAR experiment are used. The data are stored in form of PicoDst ("*.PicoDst.root") files which are ROOT-tree-like files containing information about tracks and events as reconstructed by the STAR detector. The PicoDst files in fact contain only selection of all events and tracks for easier and faster analysis by any user.

The PicoDst files are result of relatively complex data processing. The data start their path during the data taking which usually starts in February and ends in first half of July. During this period, the measurement is running non-stop every day, i.e. for 24 hours, 7 days in a week. The data for physics analysis are taken in form of so called runs. While starting a new run a selection of triggers and STAR sub-detectors are included, depending on the physics to be studied from the data. Individual runs are usually approximately 30 minutes long. Each run has its own unique number for easy identification. An example for Run14 data run number is "Run_15107005", where "15" is the year (for Run14 number 15 is used), "107" is day in the year and "005" is the number of the run in the day.

This raw data are then processed into "*.daq" files, where DAQ stands for Data Acquisition. The files are stored on HPSS (High Performance Storage System) tapes. These "*.daq" files are very large and contain a lot of information not needed for actual data analysis. For that reason the data are processed as shown in Fig. 4.1. The "*.daq" files are first moved to cental hard drive via the Data Carousel and they are marked as restored. Then the SUMS (STAR Unified Meta Scheduler) submits one file per job to a remote site where so-called MuDst (micro-Dst, "*.MuDst.root") are created from the "*.daq" files. The MuDst files are subsequently moved back to BNL to MuDst buffer from where they are, after check, moved to centralised disc at the RCF (RHIC Computing Facility) and, at the same time, they are archived on the HPSS tapes.

The MuDst files are still very large and are not very practical for data analysis. They are, for that reason, processed to the PicoDst files which contain primarily events and tracks needed for given analysis. For the analysis presented here, it was done centrally by the RNC (Relativistic Nuclear Collisions program) Soft Physics Group in Lawrence Berkeley National Laboratory, USA [50].
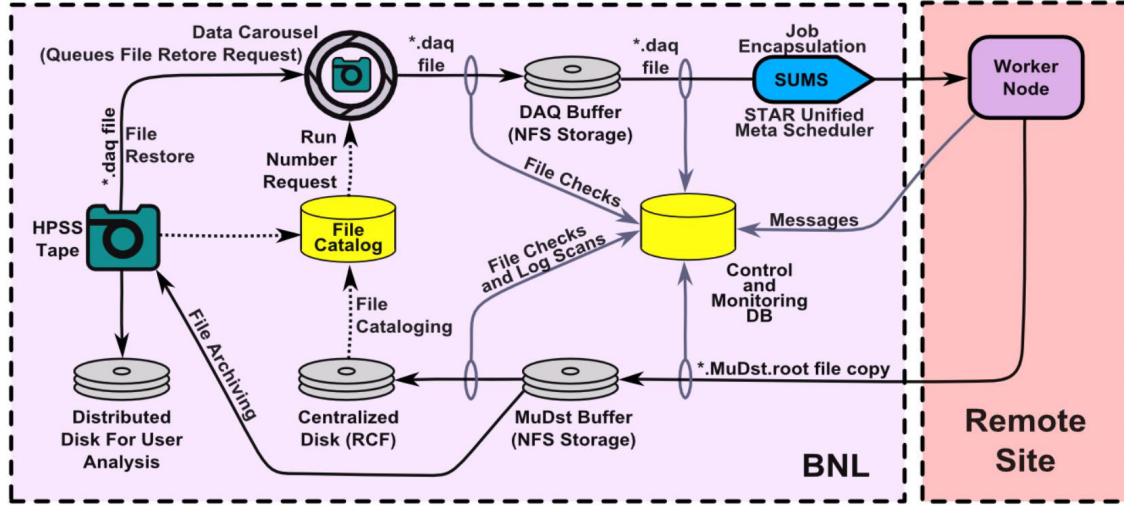
Fig. 4.1: STAR production data flow scheme. For description see the text. Taken from Ref. [51].

Event Selection	Track Selection
$(V_x, V_y, V_z) \neq (0, 0, 0)$	$0 \leq \text{flag} \leq 1{,}000$
$|V_z| < 100 \, \text{cm}$	$p_T^{(glob.)} > 0.1 \, \text{GeV}/c$
$\sqrt{V_x^2 + V_y^2} < 2 \, \text{cm}$	$\text{gDCA} < 10 \, \text{cm}$
$\text{RefMult} \geq 0$	
$|V_z - V_{zVpd}| < 3 \, \text{cm}$	

Tab. 4.1: PicoDst production event and track selection cuts. The position of the primary vertex (V_x, V_y, V_z) is determined from tracking by the TPC and the HFT, RefMult is number of charged particles reconstructed by the TPC, V_{zVpd} is position of the primary vertex along the beam axis measured by the VPD (used only when available), "flag" controls the track quality, p_T is transverse momentum and gDCA is global DCA. Taken from Ref. [50].

In case of Run14 data, only events and tracks satisfying criteria listed in Tab. 4.1 were accepted. The position of the primary vertex (V_x, V_y, V_z) is determined by the TPC and the HFT and was required to satisfy cuts in left column of Tab. 4.1. Additional event cuts are applied on the multiplicity in the TPC RefMult and difference of position of the primary vertex along the beam axis measured by TPC (V_z) and VPD (V_{zVpd}), if the information from the VPD is available. Individual tracks are constrained by cuts in the right column of Tab. 4.1. Only transverse momentum p_T, track quality "flag" and global DCA, gDCA, cuts were applied.

As a result, the PicoDst files are smaller than MuDst and so time necessary for the user analysis is noticeably reduced. The PicoDst files contain information about recorded events (individual collisions) and also information about individual tracks in given event. The data stored for events and tracks depends on triggers and detectors which were included during the data taking. For that reason, information about the triggers is also included in the PicoDst files. It is also important to note that only data suitable for physics measurement were stored, i.e. data in so-called st_physics stream. List of all available triggers is in Ref. [50].

For this analysis, triggers denoted "vpdmb-5-p-nobsmd-hlt" and "vpdmb-5-p-nobsmd" were used. This means that VPD was used as trigger detector, so-called minimum bias (MB) events are used which means that all centralities are accepted. The position of the primary vertex has to be no further than 5 cm from the detector centre which is necessary for all HFT related measurements.

All events are pile-up protected. Pile-up occurs mainly in TPC where multiple events at a time can be detected due to long read-out time. Next, the BSMD is not available with this trigger settings. And lastly, the HLT means High Level Trigger. The HLT helps with event selection during the data-taking and so reduces amount of data written to the HPSS tapes.

4.2 Non-photonic electrons analysis

NPE analysis presented in this thesis uses the DCA method. Basic ideas of this method were already introduced in sections 2.2.1 and 2.2.3, more detailed characterization is provided here. The analysis has three main stages. First is reconstruction of the inclusive electrons DCA_{xy} from the data using event and track quality cuts, second step is performing a simulation of the DCA_{xy} distributions for electrons from individual sources, including D and B mesons and photonic background, and the final stage is to fit the simulated DCA_{xy} distributions to the data. Subsequently, information about production of D mesons and B mesons can be extracted from the fit.

It is important to note that all plots and results presented in this thesis have to be considered a work-in-progress. All uncertainties are statistical. The main goal of this thesis is to understand, explain and test individual steps of the DCA analysis method of the NPE and show relevant plots for each step. The intention is to show all the steps and explain their main ideas. I would like to note that similar and independent analysis is currently performed by other STAR groups and first preliminary results were presented at QM 2017 conference.

4.2.1 Inclusive electrons from data

As already mentioned, the analysed data sample is from Run14 Au+Au at $\sqrt{s_{NN}} = 200\,\text{GeV}/c$. The source files are selection of P16id[1] Run14 PicoDst files relevant for the NPE study (only runs with correct settings of all needed STAR sub-detectors and correct trigger settings were chosen). The analysis was performed at networked distributed computing cluster called PDSF which is run by NERSC (The National Energy Research Scientific Computing Center), mainly because the PicoDst files are stored at the PDSF.

The base code for reading PicoDst files was developed by members of the STAR collaboration. This base code reads the PicoDst files event-by-event and allows access to information about particle tracks in each event. The end user adds required event, track quality and PID cuts and also code which saves the desired information about the events and tracks.

$|V_z| < 6\,\text{cm}$
$|V_z - V_{zVPD}| < 3\,\text{cm}$

Tab. 4.2: Additional event cuts to those used for PicoDst production (See Tab. 4.1). The V_z is position of the primary vertex along the beam axis reconstructed by the TPC, the V_{zVPD} is position of the primary vertex along the beam axis reconstructed by the VPD.

For this analysis, additional event cuts to those used for PicoDst production were applied and are listed in Tab. 4.2. The V_z is position of the primary vertex along the beam axis reconstructed by the TPC, the V_{zVPD} is position of the primary vertex along the beam axis reconstructed by the VPD. These cuts ensure, that the position of the primary vertex is close to the centre of the STAR detector which is necessary for track reconstruction with the HFT. To show influence of these event cuts, the distribution of $V_z - V_{zVPD}$ is presented in Fig. 4.2. From total of approx. $500 \cdot 10^6$ PicoDst events cca. $400 \cdot 10^6$ passed these additional event cuts.

After checking for good events, as described above, the code goes track-by-track for each good event. The tracks are first checked based on track quality cuts listed in Tab. 4.3. The constraints

---

[1]Designation of PicoDst data production. In this case, the production was done in the year 2016, using STAR library SL16d. This information is important for any data analysis of PicoDst files as the code for PicoDst production is updated over time.
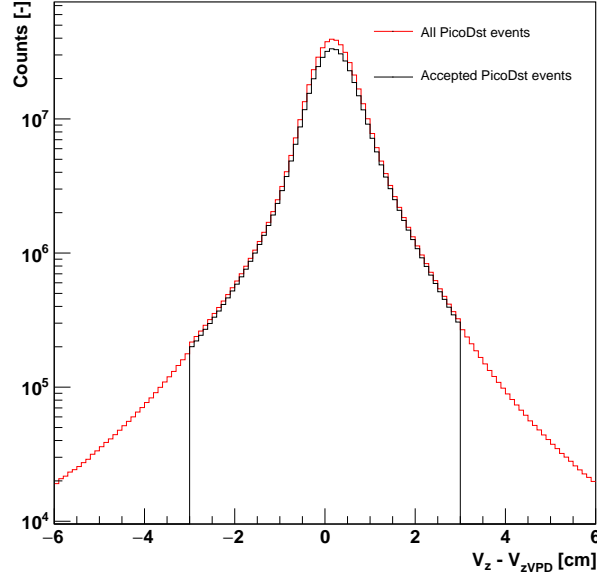
Fig. 4.2: Distribution of $V_z - V_{zVPD}$. The V_z is position of the primary vertex along the beam axis reconstructed by the TPC, the V_{zVPD} is position of the primary vertex along the beam axis reconstructed by the VPD. All PicoDst events (red) are compared to PicoDst events accepted based on additional event cuts (black).

on number of TPC points of the track nHitsFit ensures that the dE/dx resolution of approx. 8% is achieved [46]. Cut on nHitsFit/nHitsMax reduces number of split tracks, the restriction of number of fit points for dE/dx determination nHitsdEdx also improves the dE/dx resolution. Cut on pseudorapidity η ensures that the tracks are fully in acceptance of the STAR sub-detectors and that the tracking efficiency is high[2]. Restriction of global DCA, the $gDCA$, ensures that only tracks coming from primary and secondary vertices are selected and so reduces contribution of conversion electrons which occurs in material of the detector. Lower limit for p_T was used to reduce time needed for the data analysis (time the code is running) and the upper limit was chosen because there are very little number of events with tracks having $p_T > 4\,\mathrm{GeV}/c$, possibly due to used trigger.

nHitsFit > 20
nHitsFit/nHitsMax > 0.51
nHitsdEdx > 10
$\lvert \eta \rvert < 0.7$
$gDCA < 1,5\,\mathrm{cm}$
$0.4 < p_T < 4.0\,\mathrm{GeV}/c$

Tab. 4.3: Track quality cuts. The nHitsFit is number of TPC points of the track, nHits-Fit/nHitsMax is ratio of number of TPC points of given track and maximum umber of TPC points of a track, the nHitsdEdx is number of points used for PID based on dE/dx, η is pseudo-rapidity, $gDCA$ is global DCA and p_T is transverse momentum.

---

[2]The acceptance of the STAR detectors in the cental barrel is usually quoted to be $\lvert \eta \rvert < 1$. Choice of $\lvert \eta \rvert$ in Tab. 4.2 ensures that all accepted tracks are fully within acceptance of all used sub-detectors.

For identification of electrons various PID cuts were applied. For electrons with $0 < p_T < 2\,\text{GeV}/c$ combination of HFT+TPC+TOF was used, for particles with $2 \leq p_T < 4\,\text{GeV}/c$ combination of HFT+TPC+BEMC was used. This choice is related to resolution and efficiency of TOF and BEMC for particles with different p_T as described in chapter about the STAR detector. The PID cuts for both p_T intervals are listed in Tab. 4.4. The HFT and TPC cuts are here the same for both p_T intervals. The tracks were required to have one hit in each of three innermost layers of the HFT, i.e. one hit in PIXEL-1, one hit in PIXEL-2 and one hit in IST. The TPC identification was done using quantity denoted $n\sigma_e$ which can be defined (Taken from Ref. [46])

$$n\sigma_e = \ln\left[\frac{\left(\frac{\mathrm{d}E}{\mathrm{d}x}\right)_e}{B_e}\right] / \sigma_e \tag{4.1}$$

where $(\mathrm{d}E/\mathrm{d}x)_e$ is information about ionizing energy losses for electrons, B_e is the Bischel function (modified Bethe-Bloch formula) which represents theoretical prediction for ionizing energy loss in the TPC gas and σ_e is $(\mathrm{d}E/\mathrm{d}x)_e$ resolution of the TPC. The TOF identification is done by constraining particle velocity $\beta = \frac{v}{c}$. In case of electrons, the velocity is expected to be close to the speed of light. In the BEMC, the electrons are identified by ratio $\frac{p}{E_0}$, where p is particle momentum and E_0 is energy deposited in the BEMC by the particle. As electrons are light particles they most likely leave all their energy int the BEMC and so the $\frac{p}{E_0} \approx 1$. To help with the BEMC PID, cluster sizes (phiDist, zDist and TowDist = $\sqrt{\text{phiTowDist}^2 + \text{etaTowDist}^2}$) are also constrained.

HFT+TPC+TOF	HFT+TPC+BEMC
HFT required	HFT required
$-1 < n\sigma_e < 3$	$-1 < n\sigma_e < 3$
$\left\|\frac{1}{\beta} - 1\right\| < 0.025$	$0.1 < \frac{p}{E_0} < 2.0$
-	phiDist < 0.06 cm
-	zDist < 10 cm
-	TowDist < 0.02 cm

Tab. 4.4: List of electron identification cuts. For electrons with $0 < p_T < 2\,\text{GeV}/c$ combination of HFT+TPC+TOF was used, for particles with $2 \leq p_T < 4\,\text{GeV}/c$ combination of HFT+TPC+BEMC was used. For more details see the text.

Influence of cuts in Tab. 4.4 on track selection is shown in several following plots. In Fig. 4.3, there is $1/\beta$ as a function of particle momentum p from the TOF for all PicoDst tracks (from good events) in panel a) and for tracks which passed all (track quality and PID) cuts in panel b). The cuts seem to be efficient in eliminating most of the hadronic contamination. For $p > 1.6\,\text{Gev}/c$ the contamination can be clearly seen as points lying far from $1/\beta = 1$ line[3]. As will be discussed later, small hadronic contamination does not mean big problems in NPE analysis using the DCA method.

Information from the TPC can be shown in similar way. Fig. 4.4 shows charged particle energy loss $\mathrm{d}E/\mathrm{d}x$ as a function of particle momentum p. Again, panel a) shows all PicoDst tracks (from good events), panel b) shows only tracks which passed all cuts, i.e. inclusive electron candidates. More practical is to use $n\sigma_e$ than $\mathrm{d}E/\mathrm{d}x$. Distribution of $n\sigma$ from the TPC for $0 < p_T < 4\text{GeV}/c$ is shown in the Fig. 4.5. In panel a), where there are all PicoDst tracks, the electrons are not clearly visible, but in panel b), after all cuts, the electron peak emerges. In analysis without DCA, the $n\sigma$ distribution for electrons can be used for hadron contamination determination, but in analysis

---

[3]The plot is shown as a function of particle momentum p and not transverse momentum p_T. For that reason the hadronic contamination can be seen for $p < 2\,\text{GeV}/c$.
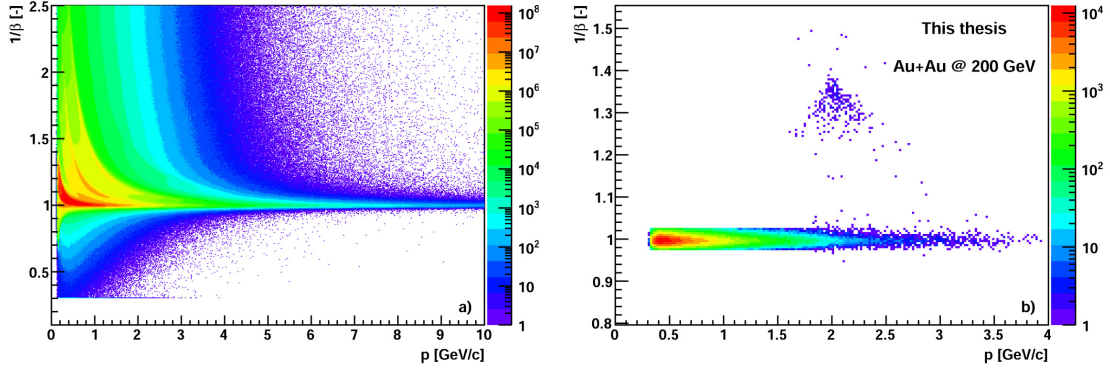
Fig. 4.3: Information about particle velocity β from the TOF. The dependency is plotted as $1/\beta$ as a function of particle momentum p. Panel a) shows all PicoDst tracks (from good events), panel b) shows only tracks which passed all cuts, i.e. inclusive electron candidates.

using DCA method the hadronic background can be determined differently. As mentioned above, this will be discussed later.
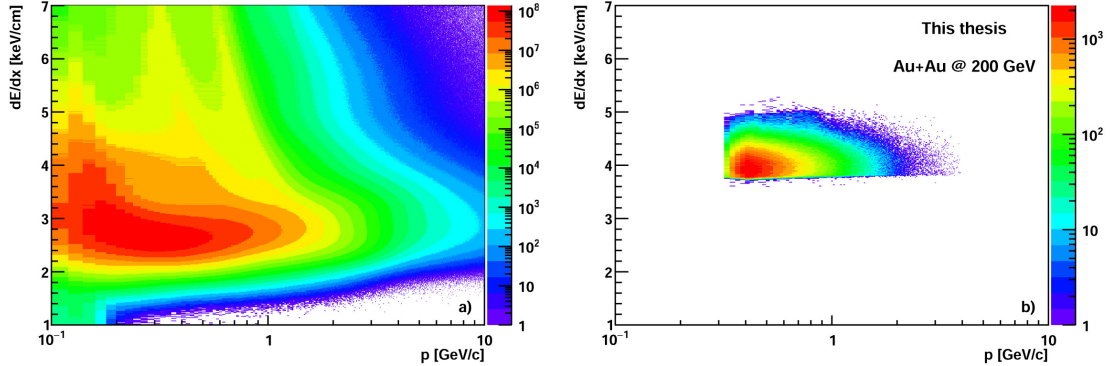

Fig. 4.4: Charged particle energy loss dE/dx as a function of particle momentum p obtained form the TPC. Panel a) shows all PicoDst tracks (from good events), panel b) shows only tracks which passed all cuts, i.e. inclusive electron candidates.

It is also good to check if the used data sample is not corrupted in some way. The check was done by plotting number of electron candidates (inclusive electrons) per event for in each day of NPE data-taking. This plot is shown in Fig. 4.6. Each bin in 4.6 was filled by fraction $\frac{N_e}{N_{evt_i}}$ where N_e is number of electron candidates measured during given day and $N_{evt.}$ is number of good events measured during given day. Ideally, this ratio should be constant over the whole period of the data-taking, but in reality it is not. The cause influence of the fluctuations on the data analysis is still under investigation and may be related to the STAR detector acceptance and performance.

To check the PID cuts, electron pairs low invariant mass M_{inv} spectrum was reconstructed and is shown in Fig. 4.7 for four electron p_T bins. The signal (black) are unlike-sign pairs (blue) minus like-sign pairs (red). This spectrum is good check of the PID cuts because at such low M_{inv} the pairs are most likely electron pairs and not pair of other charged particles. These low M_{inv} electron pairs come mainly from gamma conversion in material of the detector so relatively large number of them is eliminated by the HFT. For that reason number of the pairs is low, mainly for higher p_T bins. Additional cuts had to be applied for the M_{inv}. The invariant mass itself was restricted to $0.0 < M_{inv} < 0.4 \, \text{GeV}/c^2$ and $pairDCA < 1 \, \text{cm}$, where $pairDCA$ is the closest
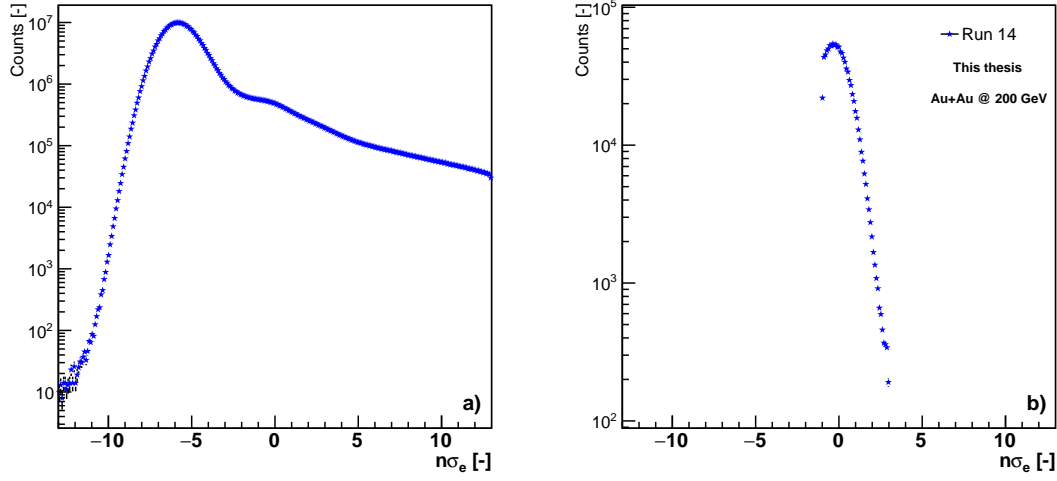
Fig. 4.5: Distribution of $n\sigma$ from the TPC for $0 < p_T < 4\,\text{GeV}/c$. Panel a) shows all PicoDst tracks (from good events), panel b) shows only tracks which passed all cuts, i.e. inclusive electron candidates.

distance between the tracks of electron and its partner. The PID cuts on (leading) electrons are listed in Tab. 4.4, for partner, only information from TPC was used (track quality cuts + $n\sigma$ cut).

It is also important to plot inclusive electrons raw yield as a function of p_T which is shown in Fig. 4.8. The spectrum is normalised by number of events $N_{evt.}$, full azimuthal angle 2π, pseudorapidity interval $d\eta$ and transverse momentum p_T. Good check of consistency of the PID cuts is here continuity of the spectrum around $p_T = 2\,\text{GeV}/c$ and also shape of the spectrum. Only points with $p_T < 4 : \text{GeV}/c$ are plotted due to used trigger settings (see trigger discussion above and Tab. 4.3).

The most important information for the NPE analysis using the DCA method are the DCA_{xy} spectra. Inclusive electrons DCA_{xy} spectra for four p_T bins are shown in Fig. 4.9. They contain contribution from decay of D and B mesons, the photonic background and also hadronic background (hadrons which passed all cuts). These spectra are to be fitted by the simulated DCA_{xy} spectra for D mesons, B mesons and photonic background. A hadronic background can be also added to the fit. As will be discussed in section 4.2.3, fitting can be reasonably performed, for data presented in this thesis, only for $1 < p_T < 2\,\text{GeV}/c$ and $2 < p_T < 3\,\text{GeV}/c$.

The template fit provides information about contribution of electrons from decay of B mesons to the total NPE yield, so called B-fraction, which is primary goal of this thesis. Such analysis, using the DCA method, does not require geometrical acceptance and detector efficiency correction, at this stage, as the result is obtained as a ratio of electrons from B and sum of electrons from D and B mesons, as will be shown in section 4.2.3. The electrons from both open heavy-flavor mesons are selected in the data analysis the same way (using the same cuts), from the same data-set. For that reason, all detector-related effects should cancel out int the ratio described above. If the data were to be compared to e.g. p+p using the R_{AA}, the acceptance and efficiency determination would be necessary.
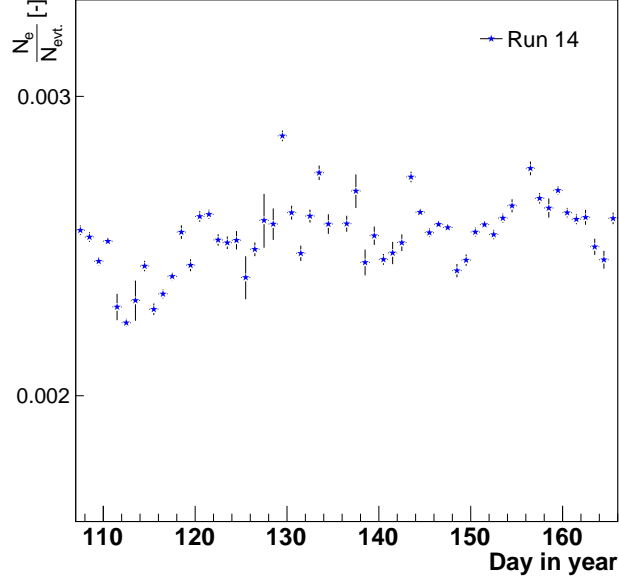
Fig. 4.6: Number of inclusive electrons per event per day in the year.
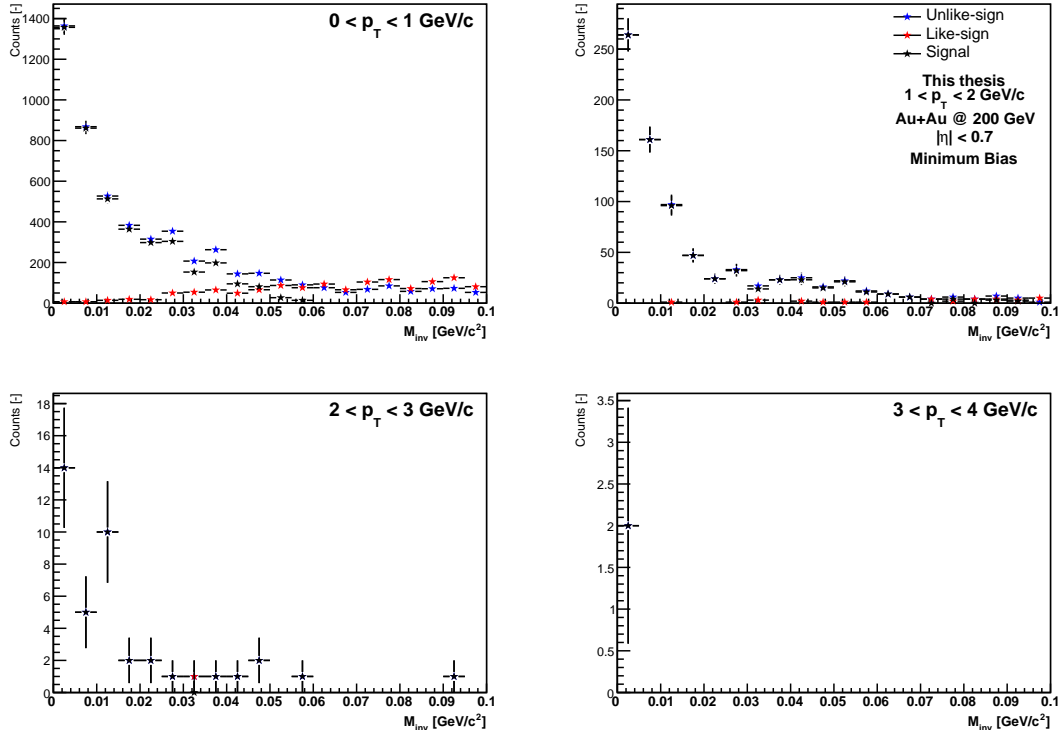
Fig. 4.7: Low invariant mass spectrum of electron pairs in four p_T bins. The signal (black) are unlike-sign pairs (blue) minus like-sign pairs (red).
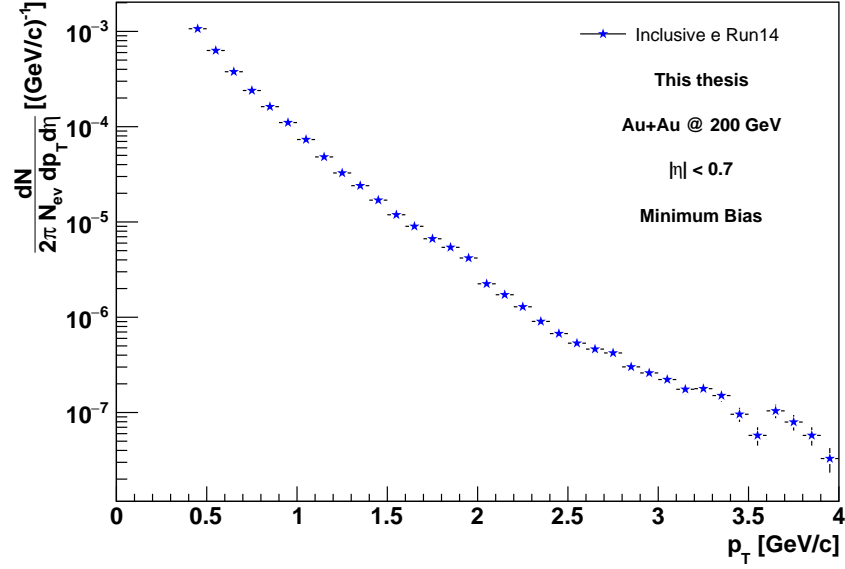
Fig. 4.8: Normalised inclusive electrons raw yield as a function of p_T. The yield is normalised by number of events $N_{evt.}$, full azimuthal angle 2π, pseudorapidity interval $\mathrm{d}\eta$ and transverse momentum p_T. The statistical errors are too little to be shown for most of the points.
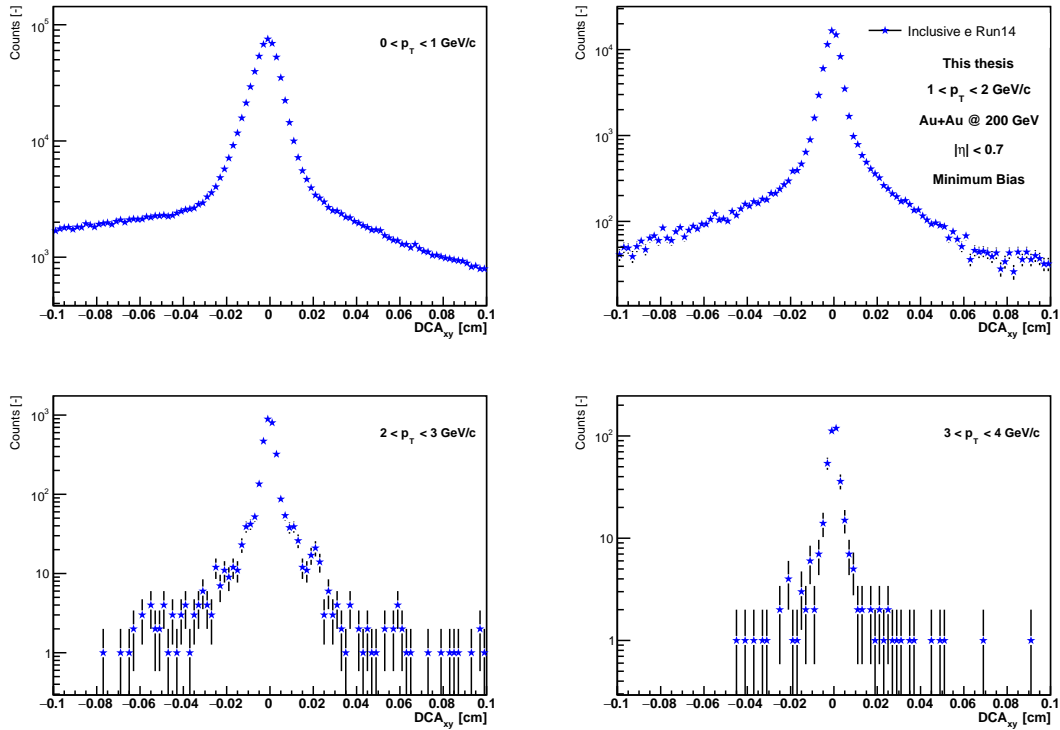
Fig. 4.9: DCA$_{xy}$ inclusive electrons spectra for four p_T bins.

4.2.2   Data-driven fast simulation

To fit distributions in Fig. 4.9, simulated templates for D mesons, B mesons and photonic background were produced. Different approach was used for D mesons with B mesons than for photonic background.

The open heavy-flavor templates were produced using EvtGen [52] + Data-driven fast simulator (FastSim). The original EvtGen, as presented in [52], was adopted by members of the STAR collaboration for purposes of STAR experiment and is usually referred as StarEvtGen. The StarEvtGen first generates kinematics of one predefined particle species and then decays it and saves information about daughter particles. In case of this analysis these pre defined particles were D^+, D^-, D^0 and B^+, B^-, B^0 mesons and only information about electrons was stored. The code is also taking into account cascade decays of B mesons which can be schematically written as $B \to D \to e$. A total of 10^7 events were generated for each of the open heavy-flavor mesons listed above. When generating mother particles, the distribution in azimuthal angle and p_T was taken to be flat, the rapidity y distribution was from PYTHIA simulation of D^0 rapidity distribution for all open heavy-flavor mesons. The FastSim then smears position of the primary vertex and momentum of the daughter particles based on information about STAR detector efficiency and acceptance. The source files for the StarEvtGen (PYTHIA y distribution) and FastSim (STAR detector efficiency and acceptance) are retaken from other D^0 study which was performed in the LBNL.

The photonic background was generated as a full HIJING simulation. Particles simulated in the HIJING were gamma (photons), π^0 and η^0 mesons. A sample of 1M events was produced by STAR NPE group. The output files of this HIJING production are PicoDst files, with similar structure as the data PicoDst. The code for reading the simulated PicoDst files was developed by STAR NPE group and saves relevant information about electron pairs, single electron production and pions. The input spectra for the HIJING simulation were just flat so the output spectra had to be reweighed for mother (gamma, π^0 and η^0) p_T using PyROOT code developed by STAR NPE group as the p_T of mother particles has influence on shape of the DCA distributions.

The final output of all simulations are three templates of the DCA_{xy}, one for D mesons (sum of D^+, D^- and D^0), one for B mesons (sum of B^+, B^- and B^0) and one for photonic background. The final simulated DCA_{xy} distributions are plotted in Fig. 4.10 in four electron p_T bins. The shape of the templates will be discussed more in the following section, but even here it can be seen that the shape of the simulated DCA_{xy} distributions for D and B mesons is very similar which is not expected result. The distribution for B mesons should be wider and lower compared to the distribution for the D mesons, due to longer B meson lifetime, as shown, for example, in Fig. 2.2 or Fig. 2.7. The main cause is most likely the flat input p_T spectrum used for generating D and B kinematics. Flat p_T is not physical so better option would be to use, for example, FONLL simulated p_T spectrum. This method is to be tested in the nearest future.
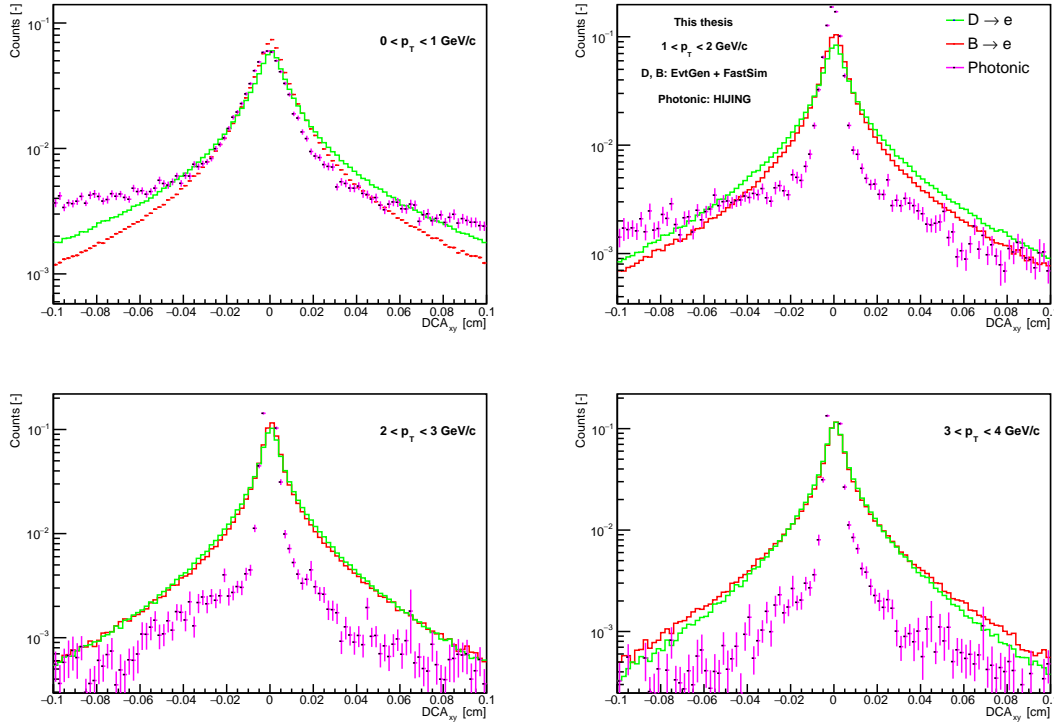
Fig. 4.10: Simulated DCA_{xy} distributions for NPE from decay of D (green) and B mesons (red) and photonic background (pink) in four electron p_T bins. For better comparison, all distributions are normalized to have integral equal to unity.

4.2.3 Template fit of the data

The templates described in previous section were fitted to the data using ROOT class TFractionFitter [53]. This class is designed exactly for purposes needed in this analysis. It takes any number of simulated histograms and fits their sum to the data histogram. The output are fractions which tell how big is contribution of individual simulated histograms to the total fit histogram and corresponding statistical error. Therefore, any fraction lies between 0 and 1. The advantage of TFractionFitter is that it is relatively simple to use, but it has problems with correct error estimation [54]. However TFractionFitter is a good tool for first fitting tests presented in this thesis.

The fitting was performed in two p_T bins, more specifically for $1 < p_T < 2\,\text{GeV}/c$ and $2 < p_T < 3\,\text{GeV}/c$. For lower p_T the fit was not done because of large miss-match effect[4], for larger p_T it was not done because of too small number of inclusive electrons in data (see Fig. 4.9).

The main challenge of the template fitting was setting the initial conditions so that the fit converges. This was ensured by scaling all (data and simulated) histograms so that their integral was equal to unity. The fit was performed with these scaled histograms. The output of the fitting is the total fit histogram and one fit parameter per each simulated histogram, i.e. three parameters in case of this analysis. Each of the parameters tells how much each simulated histogram contributes to the total fit histogram. More specifically, each parameter is ratio of simulated histogram integral and the total fit histogram integral.

The result of the fit is shown in Fig. 4.11 and Fig. 4.12. The blue points are the data (see also Fig. 4.9), the black histogram is the fit and the colored histograms are individual contributions to

---

[4]From internal discussion with STAR NPE group. Miss-math is here wrongly matched track between the TPC and the HFT.
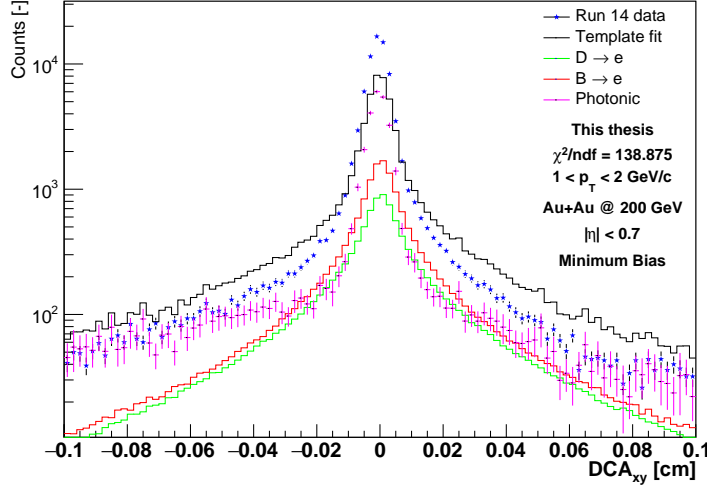
Fig. 4.11: Template fit of $\mathrm{DCA_{xy}}$ distribution for $1 < p_T < 2\,\mathrm{GeV}/c$.

the fit (see label in the plot). The fit parameters with statistical errors are listed in Tab. 4.5. As said before, the errors are very overestimated due to problems of the TFractionFitter with error calculation.

Template	$1 < p_T < 2\,\mathrm{GeV}/c$	$2 < p_T < 3\,\mathrm{GeV}/c$
$D \to e$	0.18365 ± 0.671473	0.164441 ± 0.698078
$B \to e$	0.274463 ± 0.552765	0.202952 ± 0.642846
Photonic	0.542157 ± 0.68899	0.633281 ± 0.747754

Tab. 4.5: List of fit parameters with statistical errors obtained from the template fit for both p_T bins. For description of meaning the parameters see the text.

Nevertheless, it is now possible to compute how many NPE are coming from decay of B mesons (N_{e_B}) relative to NPE coming from D and B combined ($N_{e_D} + N_{e_B}$). This means evaluating

$$\frac{N_{e_B}}{N_{e_D} + N_{e_B}}. \tag{4.2}$$

This "B-fraction" can be also calculated directly from parameters of the fit in Tab. 4.5. As described above, the parameters give fractions of the total fit histogram, i.e. fractions of total number of electrons (from simulation) $N_e^{(sim)}$. The B-fraction can be than written as

$$\frac{F_B N_e^{(sim)}}{F_D N_e^{(sim)} + F_B N_e^{(sim)}} = \frac{F_B}{F_D + F_B} \tag{4.3}$$

where F_D and F_B are the corresponding fractions of simulated histograms.

This way, the B-fraction was computed to be 0.599 for $1 < p_T < 2\,\mathrm{GeV}/c$ and 0.552 for $2 < p_T < 3\,\mathrm{GeV}/c$. The errors are not computed because of problems of TFractionFitter described above. These values clearly do not correspond with FONLL prediction and STAR and PHENIX experimental results presented in Fig. 2.8 which indicates possible problems. Due to highly overestimated errors of original histogram fractions F_B and F_D, this comparison is not, strictly speaking, relevant.
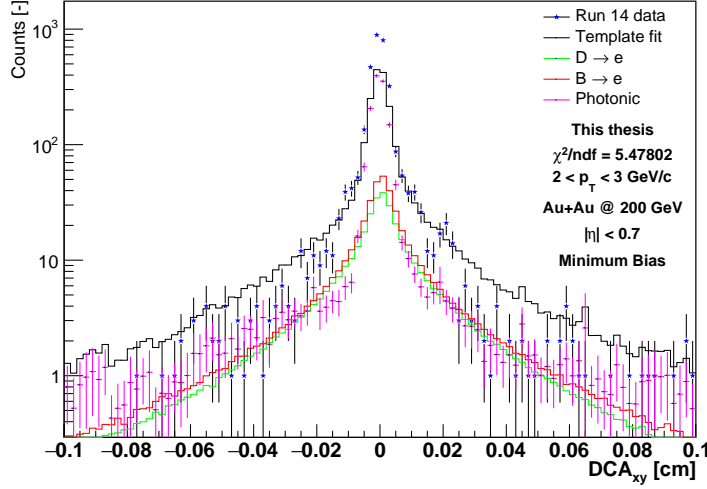
Fig. 4.12: Template fit of $\mathrm{DCA_{xy}}$ distribution for $2 < p_T < 3\,\mathrm{GeV}/c$.

At this stage, more important is to look at the fit itself. The final fit histograms and their χ^2/ndf, in Fig. 4.11 and Fig. 4.12, suggest that the fit is not correct. The most probable cause of the issue is not correct shape of the simulated templates for D and B mesons, which should look like in Fig. 2.7. This lead to (work-in-progress) result that even for low p_T there are more B mesons than D mesons detected in Au+Au collisions which is not in agreement with contemporary results.

This phenomenon was investigated and the most probable cause of the shape of D and B templates is that the D and B mesons were simulated by EvtGen with flat p_T. It turns out that the shape p_T distribution of mother particles, i.e. the D and B mesons, has major influence on the shape of NPE DCA distributions. As already discussed, the way to solve this problem is, for example, to use simulated FONLL p_T distributions as a input for generating the D and B mesons kinematics in the EvtGen[5]. This method will be tested in the nearest future in order to improve the fit and so the B-fraction value.

To improve the fit even more, a template for hadronic contamination will be added to the fit which will be obtained from the data from inclusive hadrons[6]. To obtain the B-fraction with correct values of errors, different fitting code, using the ROOT TMinuit class with χ^2 test, is under development. This method was chosen as it was proposed by the STAR NPE group as the most suitable.

---

[5]From internal discussion with STAR NPE group.

[6]Inclusive hadrons $\mathrm{DCA_{xy}}$ spectrum will be reconstructed from the same data-set used for the NPE reconstruction.

Discussion and conclusion

This thesis provides summary of analysis of the non-photonic electrons production in heavy-ion collisions. In the first chapter, a brief introduction to heavy-ion collisions was provided, the second chapter is about the main properties and experimental measurements of the open heavy-flavor mesons, in the third chapter the RHIC accelerator komplex and the STAR detector was described in context of the heavy-ion collisions and NPE measurements, and finally in the fourth and last chapter, the analysis of NPE in Run14 Au+Au collisions at $\sqrt{s_{NN}} = 200\,\mathrm{GeV}$ was described in detail.

The whole P16id Run14 Au+Au at $\sqrt{s_{NN}} = 200\,\mathrm{GeV}$ data-set dedicated for the NPE analysis was analysed and inclusive electrons candidates were selected. As DCA method was chosen, the $\mathrm{DCA_{xy}}$ distributions for the inclusive electrons were produced and were prepared for template fitting (Fig. 4.9). The consistency and correctness of applied cuts and the final distributions was checked by plotting control plots, for example electron pairs low invariant mass spectrum (Fig. 4.7) or information from TOF system (Fig. 4.3). No serious problems were identified in the final inclusive electrons selection.

The main aspect which can improve the data sample is to use different trigger settings. The data presented in this thesis used "vpdmb-5-p-nobsmd-hlt" and "vpdmb-5-p-nobsmd" triggers which contain only electron candidates with $p_T < 4\,\mathrm{GeV}$. More suitable chiose of trigger to obtain also high p_T electrons would be to use the BHT1, BHT2 and BHT3 with VPDMB (see also [50]). The BHT triggers have one additional advantage that they contain information from the SMD, in contrast to currently used ones, which helps with inclusive electron identification.

In the next step of the analysis, the $\mathrm{DCA_{xy}}$ templates for D mesons, B mesons and photonic electrons were produced. The full HIJING simulation of the photonic background and template production codes for the photonic electrons templates were provided to me by the STAR NPE group, so no issues with production of the photonic electrons templates were experienced. The templates for D and B mesons were produced using EvtGen + Data-driven fast simulator. From control plot in Fig. 4.10 and during the template fit of the data, it turned out that the shape of the D and B mesons $\mathrm{DCA_{xy}}$ templates is probably not correct. This is very likely caused by that the input p_T was taken to be just flat when generating the kinematics of the D and B mesons by the EvtGen.

It is not difficult to realise that p_T of mother particles, in this case the open heavy-flavor mesons, has major influence on the $\mathrm{DCA_{xy}}$ distributions of the electrons. Possible way to solve this problems is to use FONLL prediction of the p_T distributions for D and B mesons. Producing D and B templates with FONLL predicted p_T spectra is one of the tasks to be done in the nearest future.

The shape of the templates was examined during the final step of the NPE analysis which is the template fit. The simulated templates were fitted to the data using ROOT TFractionFitter class in two p_T bins, more specifically for $1 < p_T < 2\,\mathrm{GeV}/c$ and $2 < p_T < 3\,\mathrm{GeV}/c$. For lower p_T, the fit was not done because of large miss-match effect[7], for larger p_T it was not done because of too small number of inclusive electrons in data, as discussed above. As it turned out, the main problem, except the shape of the templates, is fact that the TFractionFitter does not compute the statistical errors correctly [54]. As a result all statistical errors computed by the TFractionFitter

---

[7]From internal discussion with STAR NPE group.

are overestimated.

So to improve the template fits, it is necessary to produce new, better templates, as already discussed and to use another fitting method. One possible way, which was also proposed by the STAR NPE group, is to use ROOT TMinuit class with χ^2 test. This method was already tested, but without success so far. The code using TMinuit $+$ χ^2 was also developed by myself, but as TMinuit is not as straightforward to use as TFractionFitter, the code requires more attention in the nearest future.

In conclusion I would like to note, again, that analogous analysis is currently in progress and is being developed by the STAR NPE group. All steps and results presented in this thesis serve as proof of principle of the NPE analysis and is a good basis for the future work to separate electrons from decay of B and D from the total NPE spectrum.

Bibliography

[1] F. Karsch, *et al.*; Thermodynamics and In-Medium Hadron Properties from Lattice QCD; 2003; arXiv:hep-lat/0305025v1.

[2] K. Yagi, *et al.*; Quark-gluon Plasma; Cambridge University Press 2005.

[3] R. Rapp, *et al.*; HIgh Density QCD nad Instantons; Annals Phys. 280 (2000) 35.

[4] Z. Fodor, *et al.*; Latice Determination of the Criical Point of QCD at Finite T and μ; JHEP 0203 (2002) 014.

[5] F. Becattini, *et al.*; Chemical Equilibrioum Study in Nucleus-Nucleus Collisions at Relativistic Energies; Phys. Rev. C69 (2004) 024905.

[6] D. H. Rischke; The Quarl-Gluon Plasma in Equilibrium; Progr. Part. Nucl. Phys. 52 (2004) 197.

[7] M. Kliemant, *et al.*; Global Properties of Nucleus-Nucleus Collisions; Lect.Notes Phys.785 (2010) 23.

[8] STAR collaboration, *et al.*; Energy Dependence of Moments of Net-proton Multiplicity Distributions at RHIC; Phys. Rev. Lett. 112 (2014) 032302.

[9] Y. Hatta, *et al.*; Proton Number Fluctuation as a Signal of the QCD Critical End-Point; Phys.Rev.Lett. 91 (2003) 102003.

[10] T. Hirano; *et al.*, Hydrodynamics and flow; 2008; arXiv:0808.2684v1 [nucl-th].

[11] B. Müller; Investigation of hot QCD matter: Theoretical aspect; 2013; arXiv:1309.7616v2 [nucl-th].

[12] F. Gelis, *et al.*; The Color Glass Condensate; Ann.Rev.Nucl.Part.Sci.60 (2010) 463.

[13] G. Roland, *et al.*, Heavy-ion collisions at the LHC, Prog.Part.Nucl.Phys. 77 (2014) 70.

[14] S. Chatrchyan, *et al.*; Study of high-p_T charged particle suppression in PbPb compared to pp collisions at $\sqrt{s_{NN}} = 2.76$ TeV; Eur. Phys. J. C 72 (2012) 1945.

[15] S. Chatrchyan, et al., Observation of sequential Upsilon suppression in PbPb collisions, Phys. Rev. Lett. 109 (2012) 222301.

[16] S. Voloshin and Y. Zhang; Flow study in relativistic nuclear collisions by Fourier expansion of Azimuthal particle distributions; Z.Phys. C70 (1996) 665-672.

[17] G. Aad, *et al.*; Measurement of the azimuthal anisotropy for charged particle production in $\sqrt{s_{NN}} = 2,76$ TeV lead-lead collisions with the ATLAS detector; Phys. Rev. C 86 (2012) 014907.

[18] B. Abelev, *et al.*; Elliptic flow of identified hadrons in Pb–Pb collisions at $\sqrt{s_{NN}} = 2,76$ TeV; CERN-PH-EP-2014-104.

[19] D. d'Enteria, B. Betz; High-p_T hadron suppression and jet quenching; Lect.Notes Phys.785:285-339; Springer 2010.

[20] STAR collaboration; Evidence from d+Au measurements for final-state suppression of high pT hadrons in Au+Au collisions at RHIC; Phys. Rev. Lett. 91 (2003) 072304.

[21] Yu. L. Dokshitzer, *et al.*; Heavy quark colorimetry of QCD matter; Phys.Lett.B519:199-206,2001.

[22] W.-Ch. Xiang, *et al.*; Radiative Energy Loss of Heavy Quark and Dead Cone Effect in Ultra-relativistic Heavy Ion Collisions; CHIN.PHYS.LETT. Vol. 22, No. 1 (2005) 72.

[23] C. Patrignani, *et al.*, (Particle Data Group); Chin. Phys. C, 40 (2016) 100001.

[24] K. OH; Measurements of Charm and Bottom Productions in Semi-leptonic Channels at STAR; poster; Quark Matter 2015, Kobe, Japan.

[25] ALICE collaboration; Measurement of electrons from beauty hadron decays in pp collisions at $\sqrt{s} = 7$ TeV; CERN-PH-EP-2012-229.

[26] ALICE collaboration; Measurement of electrons from heavy-flavour hadron decays in p-Pb collisions at $\sqrt{s_{NN}} = 5.02$ TeV; Phys. Lett. B 754 (2016) 81.

[27] ALICE collaboration; Measurement of electrons from beauty-hadron decays in p–Pb collisions at $\sqrt{s_{NN}} = 5.02$ TeV and Pb–Pb collisions at $\sqrt{s_{NN}} = 2.76$ TeV; CERN-EP-2016-222.

[28] PHENIX collaboration; Heavy Quark Production in p+p and Energy Loss and Flow of Heavy Quarks in Au+Au Collisions at $\sqrt{s_{NN}} = 200$ GeV; Phys. Rev. C 84 (2011) 044905.

[29] PHENIX collaboration; Single electron yields from semileptonic charm and bottom hadron decays in Au+Au collisions at $\sqrt{s_{NN}} = 200$ GeV; Phys.Rev. C93 (2016) no.3, 034904

[30] X. Bai; Measurements of charm and bottom production via semi-leptonic decays in Au+Au collisions at $\sqrt{s_{NN}} = 200$GeV by the STAR experiment; poster; Quark Matter 2017; Chicago, USA.

[31] O. Rusňáková; Measurements of non-photonic electrons with the STAR experiment; arXiv:1412.2112v1 [hep-ex].

[32] T. Kanesue, *et al.*; The commisioning of the laser ion source for RHIC EBIS; Proceednigs of IPAC2014, Dresden, Germany; Paper WEOAB01; p. 1890.

[33] J. Alessi, *et al.*; A hollow cathode ion source for production of primary ions for the BNL electron beam ion source, Review of scientific instruments 85 (2014) 02C107.

[34] J. G. Alessi, *et al.*; Design of EBIS for RHIC; Proceedings of the 2003 Particle Accelerator Conference; 10.1109/PAC.2003.1288848.

[35] A. Pink, *et al.*; RHIC EBIS: basic design and status of commissioning; Jinst, vol. 5, 2010.

[36] A. Schempp, *et al.*; RQF and HI accelerators for the new EBIS injdector at BNL; Particle Accelerator Conference, 2007. PAC. IEEE; 10.1109/PAC.2007.4440782

[37] M. Harrison, *et al.*; RHIC project overrview; Nuclear Instruments and Methods in Physics Research A 499 (2003) 235.

[38] Accelerator Division, Collider-Accelerator Department; RHIC Configuration Manual; 2006.

[39] Official BNL website; Online: `https://www.bnl.gov/maps/linkable_files/pdf/north_campus.pdf`; visited 23rd February 2017.

[40] W. Fischer; Run Overview of the Relativistic Heavy Ion Collider; Online: `http://www.agsrhichome.bnl.gov/RHIC/Runs/`; visited 29th April.

[41] A. J. Stevens; Conceptual Design of the RHIC Dump Core; RHIC Project, Brookhaven National Laboratory; 1995.

[42] K.H. Ackermann, *et al.*; STAR detector overview; Nuclear Instruments and Methods in Physics Research A 499 (2003) 624.

[43] D. Beavis, *et al.*; The STAR Heavy Flavor Tracker; Technical Design Report; March 15, 2011.

[44] L. Adamczyk, *et al.*; Measurement of D^0 azimuthal anisotropy at mid-rapidity in Au+Au collisions at $\sqrt{s_{NN}} = 200\,\text{GeV}$; arXiv:1701.06060v3 [nucl-ex].

[45] M. Anderson, *et al.*; The STAR Time Projection Chamber: A Unique Tool for Studying High Multiplicity Events at RHIC; Nuclear Instruments and Methods in Physics Research A 499 (2003) 659.

[46] M. Shao, *et al.*; Extensive Particle Identification with TPC and TOF at the STAR Experiment; Nucl.Instrum.Meth.A 558 (2006) 419.

[47] W. J. Llope, *et al.*; The STAR Vertex Position Detector; arXiv:1403.6855; 2014.

[48] STAR TOF collaboration; Proposal for a Large Area Time of Flight System for STAR; May 24, 2004.

[49] M. Beddo, *et al.*; The STAR Barrel Electromagnetic Calorimeter; Nuclear Instruments and Methods in Physics Research A 499 (2003) 725.

[50] RNC Soft Physics Group website; Online: `http://rnc.lbl.gov/~xdong/SoftHadron/picoDst.html`; visited 1st April 2017.

[51] L. Hajdu, *et al.*; Automated Finite State Workflow for Distributed Data Production; Journal of Physics: Conference Series 762 (2016) 012006.

[52] EvtGen Project website; Online: `http://evtgen.warwick.ac.uk`; visited 19th April 2017.

[53] ROOT Reference Guide; TFractionFitter Class Reference; Online: `https://root.cern.ch/doc/master/classTFractionFitter.html`; visited 19th April 2017.

[54] A. Nappi; A pitfall in the use of extended likelihood for fitting fractions of pure samples in a mixed sample; Comput.Phys.Commun. 180 (2009) 269.